



**HAL**  
open science

## On the Consumption of Antarctic Bottom Water in the Abyssal Ocean

Casimir de Lavergne, Gurvan Madec, Julien Le Sommer, A. J. George Nurser,  
Alberto C. Naveira Garabato

► **To cite this version:**

Casimir de Lavergne, Gurvan Madec, Julien Le Sommer, A. J. George Nurser, Alberto C. Naveira Garabato. On the Consumption of Antarctic Bottom Water in the Abyssal Ocean. *Journal of Physical Oceanography*, 2016, 46 (2), pp.635-661. 10.1175/JPO-D-14-0201.1 . hal-01274735

**HAL Id: hal-01274735**

**<https://hal.sorbonne-universite.fr/hal-01274735>**

Submitted on 16 Feb 2016

**HAL** is a multi-disciplinary open access archive for the deposit and dissemination of scientific research documents, whether they are published or not. The documents may come from teaching and research institutions in France or abroad, or from public or private research centers.

L'archive ouverte pluridisciplinaire **HAL**, est destinée au dépôt et à la diffusion de documents scientifiques de niveau recherche, publiés ou non, émanant des établissements d'enseignement et de recherche français ou étrangers, des laboratoires publics ou privés.

# On the Consumption of Antarctic Bottom Water in the Abyssal Ocean

CASIMIR DE LAVERGNE

*Sorbonne Universités (University Pierre et Marie Curie Paris 6)-CNRS-IRD-MNHN, LOCEAN Laboratory, Paris, France*

GURVAN MADEC

*Sorbonne Universités (University Pierre et Marie Curie Paris 6)-CNRS-IRD-MNHN, LOCEAN Laboratory, Paris, France, and National Oceanography Centre, Southampton, United Kingdom*

JULIEN LE SOMMER

*CNRS-Université Grenoble Alpes, Laboratoire de Glaciologie et Géophysique de l'Environnement, Grenoble, France*

A. J. GEORGE NURSER

*National Oceanography Centre, Southampton, United Kingdom*

ALBERTO C. NAVEIRA GARABATO

*University of Southampton, National Oceanography Centre, Southampton, United Kingdom*

(Manuscript received 24 September 2014, in final form 24 November 2015)

## ABSTRACT

The abyssal ocean is primarily filled by cold, dense waters formed around Antarctica and collectively referred to as Antarctic Bottom Water (AABW). At steady state, AABW must be consumed in the ocean interior at the same rate it is produced, but how and where this consumption is achieved remains poorly understood. Here, estimates of abyssal water mass transformation by geothermal heating and parameterized internal wave–driven mixing are presented. This study uses maps of the energy input to internal waves by tidal and geostrophic motions interacting with topography combined with assumptions about the distribution of energy dissipation to evaluate diapycnal transports induced by breaking internal tides and lee waves. Geothermal transformation is assessed based on a map of geothermal heat fluxes. Under the hypotheses underlying the constructed climatologies of buoyancy fluxes, the authors calculate that locally dissipating internal tides and geothermal heating contribute, respectively, about 8 and 5 Sverdrups (Sv;  $1 \text{ Sv} \equiv 10^6 \text{ m}^3 \text{ s}^{-1}$ ) of AABW consumption (upwelling), mostly north of  $30^\circ\text{S}$ . In contrast, parameterized lee wave–driven mixing causes significant transformation only in the Southern Ocean, where it forms about 3 Sv of AABW, decreasing the mean density but enhancing the northward flow of abyssal waters. The possible role of remotely dissipating internal tides in complementing AABW consumption is explored based on idealized distributions of mixing energy. Depending mostly on the chosen vertical structure, such mixing could drive 1 to 28 Sv of additional AABW upwelling, highlighting the need to better constrain the spatial distribution of remote dissipation. Though they carry large uncertainties, these climatological transformation estimates shed light on the qualitative functioning and key unknowns of the diabatic overturning.

## 1. Introduction

The abyssal ocean is primarily filled by Antarctic Bottom Water (AABW), a cold, dense water mass produced around Antarctica that spreads northward to

cover most of the World Ocean floor (Johnson 2008). While sinking and spreading along the seabed, the densest, newly formed AABW entrain and mix with ambient Southern Ocean waters to reach a maximum northward flow of about 20–30 Sverdrups (Sv;  $1 \text{ Sv} \equiv 10^6 \text{ m}^3 \text{ s}^{-1}$ ) near  $30^\circ\text{S}$  (Ganachaud and Wunsch 2000; Lumpkin and Speer 2007; Talley et al. 2003; Talley 2008, 2013). To close the abyssal overturning circulation and reach a steady state, the northward-flowing AABW

---

*Corresponding author address:* Casimir de Lavergne, LOCEAN Laboratory, 4 Place Jussieu, F-75005 Paris, France.  
E-mail: casimir.delavergne@gmail.com

must gain buoyancy and upwell across isopycnals in the Pacific, Indian, and Atlantic basins. In the deep ocean, this buoyancy gain can only be achieved through two processes: mixing and geothermal heating. Were the cold bottom waters not consumed by such diabatic processes, they would gradually fill the whole ocean interior. In contrast, the overlying, southward-flowing deep waters may upwell mostly adiabatically in the Antarctic Divergence, allowing their consumption to rely largely on near-surface transformation (Toggweiler and Samuels 1995; Talley 2013).

Downward diffusion of buoyancy by turbulent mixing is considered to be the dominant mechanism allowing for AABW consumption and, thereby, for the maintenance of the abyssal stratification (Munk and Wunsch 1998; Wunsch and Ferrari 2004). The required diapycnal mixing is thought to be primarily driven by the breaking of internal waves. These ubiquitous waves in the ocean interior derive their energy from winds and tides and generate turbulence when they become unstable and break (Garrett and Munk 1979). Baroclinic tide and lee wave generation by tidal and geostrophic flows impinging on rough topography are among the most significant sources of internal wave energy for the deep ocean (Egbert and Ray 2000; Garrett and St. Laurent 2002). Some of these internal waves tend to break near their generation sites and contribute to mixing in the near field, whereas low-mode waves are able to propagate over large distances and may dissipate in the far field (St. Laurent and Garrett 2002).

According to a recent calculation (Nikurashin and Ferrari 2013), mixing driven by locally dissipating internal tides and lee waves is able to drive 25 Sv of AABW upwelling globally and could therefore account for the full strength of the abyssal overturning. Yet, experiments with ocean general circulation models (OGCM) have shown less of an impact of parameterized near-field mixing from internal tides and lee waves: only about 5 and 2 Sv of additional abyssal flow was simulated with the successive inclusion of near-field tidal mixing and lee wave-driven mixing (Simmons et al. 2004; Saenko and Merryfield 2005; Melet et al. 2014). In a recent OGCM study (Oka and Niwa 2013), it was suggested that the addition of far-field tidal mixing—that is, mixing driven by remotely dissipating internal tides—is key in simulating a Pacific overturning circulation of realistic strength. Meanwhile, although most studies focus on diapycnal mixing as the main buoyancy supply for AABW, geothermal heating was shown to be a rivalling heat source for the bottom-most waters of the ocean (Emile-Geay and Madec 2009). Indeed, it has been estimated that 2 to 6 Sv of abyssal flow may be sustained by geothermal heat fluxes alone (Adcroft et al. 2001; Hofmann and Morales Maqueda 2009; Emile-Geay and Madec 2009). These recent disparate results show that it remains largely unclear which

processes control the strength of the lower branch of the overturning and how and where the diabatic return of northward-flowing bottom waters is accomplished.

In the past decades, much attention has been directed to the identification of mechanical energy sources able to sustain sufficient internal wave activity and deep mixing. Munk and Wunsch (1998) calculated that 2.1 TW are required to upwell 30 Sv of dense waters across isopycnals from 4000- to 1000-m depth. Considering that AABW need only upwell until it joins the southward adiabatic route to the Southern Ocean outcrop region (Talley 2013), this number could be substantially reduced. On the other hand, deep-ocean power availability from tides and lee-wave radiation has been estimated as 0.9–1.3 (Egbert and Ray 2000; Nycander 2005; Melet et al. 2013b) and 0.15–0.75 TW (Scott et al. 2011; Nikurashin and Ferrari 2011; Wright et al. 2014; Nikurashin et al. 2014), respectively. But though these global estimates of power availability and requirement may compare favorably, they do not discriminate between different water masses, despite different return pathways. Indeed, differing spatial distributions of wave-breaking energy can have radically different implications for ocean circulation (Simmons et al. 2004; Saenko et al. 2012; Oka and Niwa 2013).

The water mass transformation framework (Walin 1982; Nurser et al. 1999; Marshall et al. 1999; Iudicone et al. 2008b) enables us to translate the energy available for mixing into diapycnal transports that can be meaningfully compared to rates of dense water input. Here, we address some of the questions regarding AABW consumption by evaluating climatological rates of water mass conversion in the ocean interior by internal wave breaking and geothermal heating. We describe the water mass transformation framework and the dataset employed in the following section. In section 3, we outline some qualitative properties of diapycnal transports induced by mixing and geothermal heating and justify the choice of the  $28.11 \text{ kg m}^{-3}$  neutral surface as the upper boundary of AABW based on the climatological density structure of the ocean. Transformation estimates are presented in section 4. Results from earlier and present studies are compared and reconciled in section 5. Conclusions make up the last section. Further discussion on the role of nonlinearities in the equation of state and on the importance of hypsometry for water mass transformation can be found in appendixes A and B, respectively.

## 2. Methods

### *a. Water mass transformation in the neutral density framework*

We denote by  $K_{\perp}$  and  $K_{\parallel}$  the turbulent diapycnal and isopycnal diffusivities, respectively. For a given oceanic

property  $\lambda$ , we define the diapycnal diffusive flux of  $\lambda$  as  $F^\lambda = K_\perp \partial_\perp \lambda$ , where  $\partial_\perp$  is the gradient along the diapycnal direction. The isopycnal diffusive flux of  $\lambda$  is given by  $K_\parallel \nabla_\parallel \lambda$ , with  $\nabla_\parallel$  as the spatial gradient in the tangent isopycnal plane. In a reference frame that follows instantaneous isopycnals and in the absence of external forcings from the surface, the rate of change of the locally referenced potential density  $\rho$  due to diffusive fluxes of Conservative Temperature  $\Theta$  and Absolute Salinity  $S_A$  must be balanced by the advection across isopycnals (McDougall 1984; Iudicone et al. 2008b):

$$\begin{aligned} \omega \partial_\perp \rho = & \partial_\Theta \rho [\partial_\perp F^\Theta + \nabla_\parallel \cdot (K_\parallel \nabla_\parallel \Theta)] \\ & + \partial_{S_A} \rho [\partial_\perp F^{S_A} + \nabla_\parallel \cdot (K_\parallel \nabla_\parallel S_A)], \end{aligned} \quad (1)$$

where we have introduced the diapycnal velocity  $\omega$ . Note that, by convention, the diapycnal axis is oriented from low to high density, so that  $\omega > 0$  corresponds to transport toward greater densities. For brevity, Conservative Temperature and Absolute Salinity will be referred to simply as “temperature” and “salinity” in all the following.

Water mass transformation by isopycnal mixing was estimated by Iudicone et al. (2008a,b) and Klocker and McDougall (2010), who showed that isopycnal diffusion results in significant net densification in the Southern Ocean, contributing to the production of abyssal waters but not to their consumption. Here, we focus on the consumption of AABW by internal wave–driven diapycnal mixing and geothermal heating and only diagnose the contribution of diapycnal mixing terms to the diapycnal velocity:

$$\omega \partial_\perp \rho = \partial_\Theta \rho \partial_\perp F^\Theta + \partial_{S_A} \rho \partial_\perp F^{S_A}. \quad (2)$$

Since neutral surfaces are tangent to local isopycnal surfaces by construction, the diapycnal velocity  $\omega$  equates the local dianeutral velocity (Jackett and McDougall 1997). By integrating  $\omega$  over a given neutral surface  $A(\gamma)$ , with  $\gamma$  neutral density, one obtains the total dianeutral transport or transformation rate  $T(\gamma)$  (Walin 1982):

$$\begin{aligned} T(\gamma) &= \iint_{A(\gamma)} \omega \, dA \\ &= \iint_{A(\gamma)} (\partial_\perp \rho)^{-1} (\partial_\Theta \rho \partial_\perp F^\Theta + \partial_{S_A} \rho \partial_\perp F^{S_A}) \, dA. \end{aligned} \quad (3)$$

Equation (3), though exact and relatively simple, is difficult to implement in a discrete calculation. To avoid sampling issues, reduce data noise, and allow more detailed diagnostics, we take advantage of the global character of neutral density to propose an equivalent,

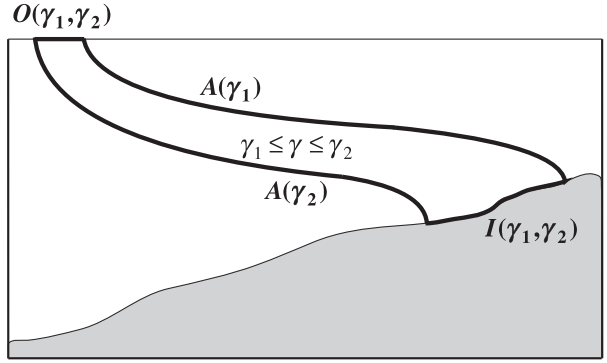


FIG. 1. Sketch of a neutral density layer  $\gamma_1 \leq \gamma \leq \gamma_2$  bounded by neutral surfaces  $A(\gamma_1)$  and  $A(\gamma_2)$  and by its outcrop and incrop surfaces  $O(\gamma_1, \gamma_2)$  and  $I(\gamma_1, \gamma_2)$ .

more robust formulation for computing the dianeutral transports. Multiplying (2) by the factor  $b = \partial_\perp \gamma / \partial_\perp \rho$  (Iudicone et al. 2008b), we obtain the neutral density balance

$$\omega \partial_\perp \gamma = b \partial_\Theta \rho \partial_\perp F^\Theta + b \partial_{S_A} \rho \partial_\perp F^{S_A}. \quad (4)$$

From here, two different directions may be taken.

The simplest approach consists of neglecting spatial variations of the coefficients  $b \partial_\Theta \rho$  and  $b \partial_{S_A} \rho$  (i.e., neglecting effects related to the nonlinearity of the equation of state), allowing the diapycnal velocity to be expressed as

$$\begin{aligned} \omega^{\text{lin}} &= (\partial_\perp \gamma)^{-1} \partial_\perp (b \partial_\Theta \rho F^\Theta + b \partial_{S_A} \rho F^{S_A}) \\ &= \partial_\gamma (b \partial_\Theta \rho F^\Theta + b \partial_{S_A} \rho F^{S_A}). \end{aligned} \quad (5)$$

Noting that  $b \partial_\Theta \rho F^\Theta + b \partial_{S_A} \rho F^{S_A} = b F^\rho = F^\gamma$ , (5) reduces to  $\omega^{\text{lin}} = \partial_\gamma F^\gamma$ , giving

$$T^{\text{lin}}(\gamma) = \iint_{A(\gamma)} \partial_\gamma F^\gamma \, dA. \quad (6)$$

Since the area of integration  $A(\gamma)$  depends on  $\gamma$ , care must be taken when moving the  $\gamma$  derivative in (6) outside of the integral. Consider a neutral density layer  $V(\gamma_1, \gamma_2)$  defined by  $\gamma_1 \leq \gamma \leq \gamma_2$  (Fig. 1). The layer will intersect the surface and bottom of the ocean over two distinct surfaces, which we denote by  $O(\gamma_1, \gamma_2)$  and  $I(\gamma_1, \gamma_2)$  and refer to as the outcrop and incrop surfaces, respectively. Together with  $A(\gamma_1)$  and  $A(\gamma_2)$ , these surfaces bound the considered layer volume. Using these definitions and Leibniz’s integral rule, we obtain

$$\begin{aligned} T^{\text{lin}}(\gamma) &= \partial_\gamma \iint_{A(\gamma)} F^\gamma \, dA + \partial_\gamma \iint_{O(\gamma, +\infty)} F^\gamma \, dA \\ &\quad - \partial_\gamma \iint_{I(\gamma, +\infty)} F^\gamma \, dA. \end{aligned} \quad (7)$$

Note that  $A(\gamma)$ ,  $O(\gamma, +\infty)$ , and  $I(\gamma, +\infty)$  enclose the volume of waters denser than  $\gamma$ , so that, using Gauss's theorem, one may also recast  $T^{\text{lin}}$  in terms of the volume-integrated divergence of the neutral density flux  $F^\gamma$ :

$$T^{\text{lin}}(\gamma) = -\partial_\gamma \iiint_{V(\gamma, +\infty)} \partial_\perp F^\gamma dV. \quad (8)$$

The discrete form of (7) reads

$$\begin{aligned} T^{\text{lin}}(\gamma)\Delta\gamma &= \iint_{A[\gamma+(\Delta\gamma/2)]} F^\gamma dA - \iint_{A[\gamma-(\Delta\gamma/2)]} F^\gamma dA \\ &\quad - \iint_{O[\gamma-(\Delta\gamma/2), \gamma+(\Delta\gamma/2)]} F^\gamma dA \\ &\quad + \iint_{I[\gamma-(\Delta\gamma/2), \gamma+(\Delta\gamma/2)]} F^\gamma dA, \end{aligned} \quad (9)$$

where  $\Delta\gamma$  is a small but finite density step. Implementation of (9) now solely requires the specification of surface and bottom boundary conditions. Since we only consider mixing in the ocean interior, air-sea exchanges are excluded and our surface boundary condition is  $F^\Theta|_{\text{surf}} = 0$  and  $F^{S_A}|_{\text{surf}} = 0$ , implying  $F^\gamma|_{\text{surf}} = 0$ . At the ocean bottom, the diffusive salinity flux must vanish,  $F^{S_A}|_{\text{bot}} = 0$ , but the diffusive temperature flux must meet the geothermal boundary condition  $F^\Theta|_{\text{bot}} = Q_{\text{geo}}/(\rho c_p^0)$ , where  $Q_{\text{geo}}$  ( $\text{W m}^{-2}$ ) is the geothermal heat flux, and  $c_p^0$  is the appropriate (constant) heat capacity. The transformation rate  $T^{\text{lin}}$  can then be decomposed into contributions of mixing and geothermal heating:

$$\begin{aligned} T_{\text{mix}}^{\text{lin}}(\gamma)\Delta\gamma &= \iint_{A[\gamma+(\Delta\gamma/2)]} F^\gamma dA \\ &\quad - \iint_{A[\gamma-(\Delta\gamma/2)]} F^\gamma dA, \quad \text{and} \end{aligned} \quad (10)$$

$$\begin{aligned} T_{\text{geo}}^{\text{lin}}(\gamma)\Delta\gamma &= \iint_{I[\gamma-(\Delta\gamma/2), \gamma+(\Delta\gamma/2)]} F^\gamma dA \\ &= - \iint_{I[\gamma-(\Delta\gamma/2), \gamma+(\Delta\gamma/2)]} \frac{b\alpha Q_{\text{geo}}}{c_p^0} dA, \end{aligned} \quad (11)$$

where we have introduced the thermal expansion coefficient  $\alpha = -\partial_\Theta \rho / \rho$  in (11). Note that, in view of the ocean aspect ratio,  $F^\gamma$  is very well approximated by  $-K_\perp \partial_z \gamma$  (e.g., Iudicone et al. 2008b), where height  $z$  increases upward and has its origin at the surface. The term  $T_{\text{mix}}^{\text{lin}}$  can therefore be computed as

$$\begin{aligned} T_{\text{mix}}^{\text{lin}}(\gamma)\Delta\gamma &= \iint_{A[\gamma-(\Delta\gamma/2)]} K_\perp \partial_z \gamma dA \\ &\quad - \iint_{A[\gamma+(\Delta\gamma/2)]} K_\perp \partial_z \gamma dA. \end{aligned} \quad (12)$$

Nonlinearity in the equation of state need not be neglected, however. Noting again that diapycnal gradients are well approximated by vertical gradients, we can integrate the neutral density tendency at the right-hand side of (4) from the seafloor ( $z = -H$ ) to the level of a given neutral surface [ $z = z_{A(\gamma)}$ ] to obtain an equivalent diffusive flux of neutral density  $F_{\text{eq}}^\gamma$  across  $A(\gamma)$ :

$$F_{\text{eq}}^\gamma(\gamma) = - \int_{-H}^{z_{A(\gamma)}} [b\partial_\Theta \rho \partial_z (K_\perp \partial_z \Theta) + b\partial_{S_A} \rho \partial_z (K_\perp \partial_z S_A)] dz. \quad (13)$$

The flux  $F_{\text{eq}}^\gamma$  represents the actual neutral density flux crossing the surface  $A(\gamma)$  as a result of turbulent diapycnal mixing of salinity and temperature below the level of  $A(\gamma)$ , accounting for the full nonlinearity of the equation of state. Equating  $\partial_\perp$  with  $-\partial_z$ , we have by construction  $\partial_\perp F_{\text{eq}}^\gamma = b\partial_\Theta \rho \partial_\perp F^\Theta + b\partial_{S_A} \rho \partial_\perp F^{S_A}$ , so that (4) becomes  $\omega = (\partial_\perp \gamma)^{-1} \partial_\perp F_{\text{eq}}^\gamma = \partial_\gamma F_{\text{eq}}^\gamma$  and

$$T(\gamma) = \iint_{A(\gamma)} \partial_\gamma F_{\text{eq}}^\gamma dA. \quad (14)$$

Replacing  $F^\gamma$  by  $F_{\text{eq}}^\gamma$  in (7)–(9) gives continuous and discrete equivalents of (14). The bottom boundary condition is unchanged and

$$T_{\text{geo}}(\gamma)\Delta\gamma = T_{\text{geo}}^{\text{lin}}(\gamma)\Delta\gamma = - \iint_{I[\gamma-(\Delta\gamma/2), \gamma+(\Delta\gamma/2)]} \frac{b\alpha Q_{\text{geo}}}{c_p^0} dA. \quad (15)$$

While surface diffusive fluxes of salinity and temperature remain set to zero, the equivalent surface flux of neutral density may now differ significantly from zero (mixing in the ocean interior may be a net source or sink of volume and of volume-integrated neutral density). The dianeutral transport induced by diapycnal mixing is thus obtained as

$$\begin{aligned} T_{\text{mix}}(\gamma)\Delta\gamma &= \iint_{A[\gamma+(\Delta\gamma/2)]} F_{\text{eq}}^\gamma dA \\ &\quad - \iint_{A[\gamma-(\Delta\gamma/2)]} F_{\text{eq}}^\gamma dA \\ &\quad - \iint_{O[\gamma-(\Delta\gamma/2), \gamma+(\Delta\gamma/2)]} F_{\text{eq}}^\gamma dA, \end{aligned} \quad (16)$$

where the last term's integrand is

$$F_{\text{eq}}^\gamma|_{\text{surf}} = - \int_{-H}^0 [b\partial_\Theta \rho \partial_z (K_\perp \partial_z \Theta) + b\partial_{S_A} \rho \partial_z (K_\perp \partial_z S_A)] dz.$$

In practice, to avoid irrelevant nonlinear effects resulting from strong diffusivities but finite  $\partial_\Theta \rho$  and  $\partial_{S_A} \rho$  gradients in unstratified surface waters [see (20) and appendix A], the no-flux surface boundary condition ( $F^\Theta|_{\text{surf}} = 0$  and  $F^{S_A}|_{\text{surf}} = 0$ ) is matched by linearly

reducing  $F^\ominus$  and  $F^{SA}$  to zero from the base of the mixed layer to the surface. This procedure is justified since we are interested in interior rather than near-surface transformation, thus excluding mixed layer processes, and since diapycnal gradients may no longer be accurately diagnosed as vertical gradients within vanishing stratification.

For diagnostic purposes, it is useful to rewrite the diapycnal transports  $T_{\text{mix}}$  and  $T_{\text{geo}}$  as the  $\gamma$  derivative of a total buoyancy flux into the volume of waters denser than  $\gamma$ . From (7), we identify

$$T_{\text{geo}}(\gamma) = \partial_\gamma \iint_{I(\gamma, +\infty)} (-F_{\text{eq}}^\gamma) dA, \quad \text{and} \quad (17)$$

$$T_{\text{mix}}(\gamma) = \partial_\gamma \iint_{A(\gamma) \cup O(\gamma, +\infty)} F_{\text{eq}}^\gamma dA. \quad (18)$$

In (17) and (18),  $I(\gamma, +\infty)$  and  $A(\gamma) \cup O(\gamma, +\infty)$  correspond to the areas bounding the volume  $V(\gamma, +\infty)$  from below and from above, respectively.

*b. Climatologies*

Annual climatologies of the required hydrographic properties, including neutral density, are taken from the World Ocean Circulation Experiment hydrographic atlas (Gouretski and Koltermann 2004). All variables are computed according to the International Thermodynamic Equation of Seawater—2010 (TEOS-10) framework (McDougall and Barker 2011).

A climatological distribution of the energy lost to the internal wave field  $\varepsilon_T$  ( $\text{W kg}^{-1}$ ) is constructed from published estimates of energy fluxes into baroclinic tides (Nycander 2005; Melet et al. 2013b; Fig. 2a) and lee waves (Scott et al. 2011; Fig. 2b) combined with the near-field mixing parameterization of St. Laurent et al. (2002):

$$\begin{aligned} \varepsilon_T(x, y, z) = & \frac{1}{\rho} [q_{\text{LW}} E_{\text{LW}}(x, y) + q_{\text{IT}} E_{\text{IT}}(x, y) \\ & + q_{\text{ITAH}} E_{\text{ITAH}}(x, y)] \frac{\exp\{-[H(x, y) - z]/\zeta\}}{\zeta \{1 - \exp[-H(x, y)/\zeta]\}}. \end{aligned} \quad (19)$$

Parameterization (19) assumes that a fixed fraction  $q$  of generated internal waves contributes to near-field mixing and that the dissipating energy decays exponentially from the seabed with an  $e$ -folding length  $\zeta$ . Here,  $E_{\text{LW}}$ ,  $E_{\text{IT}}$ , and  $E_{\text{ITAH}}$  ( $\text{W m}^{-2}$ ) designate the power input to internal waves by geostrophic currents impinging on small-scale topography and by barotropic tidal flows interacting with topographic features of horizontal scales larger ( $E_{\text{IT}}$ ) and smaller ( $E_{\text{ITAH}}$ ) than 10 km, respectively. Topographic roughness at scales smaller than 10 km is

dominated by abyssal hills, and though it is not deterministically resolved in current global bathymetric products, its contribution to internal tide generation has been recently estimated (Melet et al. 2013b) following the methodology of Nycander (2005). The barotropic to baroclinic conversion by abyssal hill roughness, with a global energy flux of 0.1 TW, represents a nonnegligible contribution to tidal mixing and will therefore be included in our water mass transformation estimates. The  $q_{\text{LW}}$ ,  $q_{\text{IT}}$ , and  $q_{\text{ITAH}}$  parameters represent the fraction of the predicted internal wave generation power that dissipates close to generation sites, assumed to be constant in space for each flux. In the case of lee waves, which are stationary and thereby expected to dissipate only in the near field, the choice of a coefficient  $q_{\text{LW}} < 1$  is justified by observational (Sheen et al. 2013; Waterman et al. 2013, 2014) and modeling (Nikurashin and Ferrari 2010a,b; Nikurashin et al. 2014) results showing that the predicted energy fluxes (Scott et al. 2011) tend to overestimate the water column dissipation by about a factor of 3 to 10.

Falahat et al. (2014) calculated that, on a global average, the first two vertical normal modes take up 59% of the energy flux into internal tides. Since near-field dissipation is thought to be quasi negligible for the lowest two modes, this places an upper bound for  $q_{\text{IT}}$  at 41%. On the other hand, the global data analysis of Waterhouse et al. (2014) suggests a minimum of 20% of local internal tide dissipation. Because small-scale bathymetry tends to favor the generation of small-scale, high-mode waves, a somewhat larger portion of local dissipation should apply to internal tides generated by abyssal hills, so that  $q_{\text{ITAH}} \sim 0.5$  may be considered a reasonable reference value (A. Melet 2014, personal communication). The parameter  $q_{\text{LW}}$  is less well constrained, with a probable range of about 0.1–0.5 (Nikurashin and Ferrari 2010a,b; Sheen et al. 2013; Waterman et al. 2013, 2014; Nikurashin et al. 2014). Near-field dissipation is generally observed to decrease away from the seafloor with a decay scale ranging roughly between 300 and 1000 m (St. Laurent et al. 2002; St. Laurent and Nash 2004; Nikurashin and Ferrari 2010a,b). To allow comparison with earlier studies, we choose typical values  $q_{\text{LW}} = q_{\text{IT}} = 1/3$  and  $\zeta = 500$  m, and we set  $q_{\text{ITAH}} = 1/2$ .

We note that both  $q$  and the vertical structure of local dissipation must vary regionally depending on topographic and oceanographic conditions (St. Laurent and Garrett 2002; St. Laurent and Nash 2004; Polzin 2009; Nikurashin and Ferrari 2010a,b; Nikurashin and Legg 2011; Waterman et al. 2013, 2014; Nikurashin et al. 2014; Falahat et al. 2014). Though the present choices for  $q_{\text{LW}}$ ,  $q_{\text{IT}}$ , and  $q_{\text{ITAH}}$  aim to be representative of global

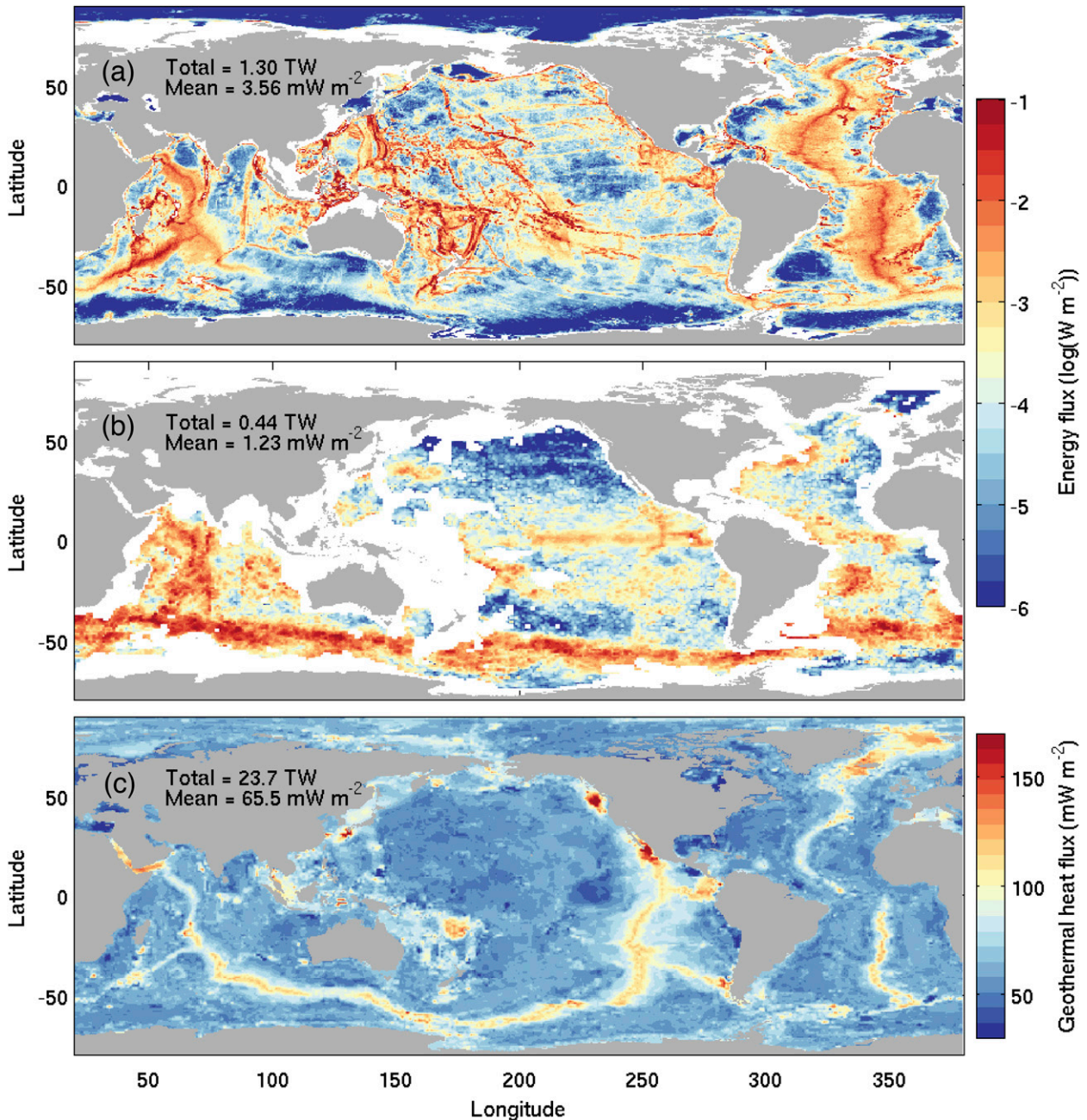


FIG. 2. Energy flux [ $\log(\text{W m}^{-2})$ ] into (a) internal tides (Nycander 2005; Melet et al. 2013b) and (b) lee waves (Scott et al. 2011). (c) Geothermal heat fluxes ( $\text{mW m}^{-2}$ ) into the bottom ocean estimated by Goutorbe et al. (2011). Mean and globally integrated fluxes are indicated in the upper-left corner of each panel. The energy flux shown in (a) includes internal tide generation by topographic features with horizontal scales larger (Nycander 2005) and smaller (Melet et al. 2013b) than 10 km.

average values, they should be viewed as a somewhat arbitrary reference, facilitating comparison with earlier work (e.g., Simmons et al. 2004; Saenko and Merryfield 2005; Nikurashin and Ferrari 2013; Melet et al. 2014) while oversimplifying the energy partitioning of the real ocean. Nonetheless, the diagnosed diapycnal transports depend linearly on the chosen  $q$  values, and local-scale

deviations from global averages should not strongly affect the general picture of the presented transformation estimates. On the other hand, because of the nonlinear dependence on  $\zeta$ , we will examine the sensitivity of transformation rates to the vertical decay scale. Though we do not test alternative, nonexponential vertical distributions of local dissipation (e.g., Polzin 2009; Melet

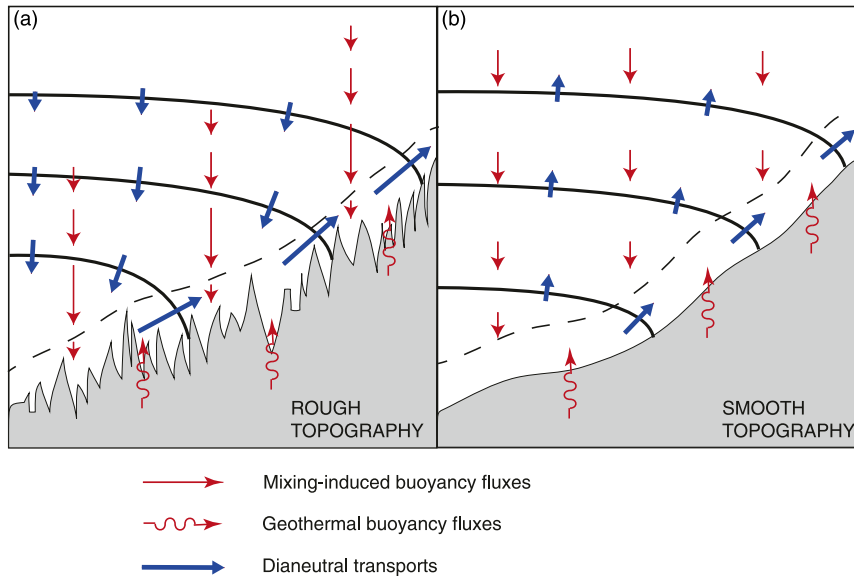


FIG. 3. Idealized schematic of local dianeutral transports induced by geothermal heat fluxes and internal wave breaking above (a) rough or (b) smooth bathymetry. In (a), the thin red arrows depict local downward buoyancy fluxes associated with bottom-intensified mixing parameterized by (19) and (20), accounting for their sharp decay in a relatively thin bottom layer (dashed line) of reduced mixing efficiency. The induced large-scale dianeutral transports (thick blue arrows) are directed toward higher (lower) density outside (within) the bottom layer. Thick black lines represent selected neutral surfaces. In (b), as a comparison example, buoyancy fluxes and dianeutral transports resulting from weaker internal wave activity and decreasing energy dissipation with depth are sketched. In this chosen situation, dianeutral upwelling occurs everywhere in the water column but preferentially along the seafloor. Note that we plot buoyancy fluxes as straight vertical arrows instead of dianeutral arrows so as to visualize the regions of divergent vs convergent buoyancy flux and to be consistent with the present methods where local density fluxes are approximated as vertical.

et al. 2013a), varying  $\zeta$  should give some indication of the robustness of the diagnosed transports.

The turbulent diffusivity can be related to the buoyancy frequency  $N^2 = -(g/\rho)\partial_z\rho$  and wave-breaking energy  $\varepsilon_T$  according to (Osborn 1980)

$$K_{\perp}N^2 = R_f\varepsilon_T, \quad (20)$$

where  $R_f$  is the mixing efficiency, taken to be one-sixth. Note that  $R_f = 1/6$  corresponds to a flux coefficient  $\Gamma = (K_{\perp}N^2)/(\varepsilon_T - K_{\perp}N^2) = 0.2$ , the canonical upper-bound value postulated by Osborn (1980). Because mixing efficiency should approach zero in unstratified waters, we must remedy for unrealistically large values of the predicted eddy diffusivity in weak stratification. Therefore, following Simmons et al. (2004),  $K_{\perp}$  is computed as

$$K_{\perp} = \min \left\{ \left[ \frac{R_f\varepsilon_T}{\max(N^2, 10^{-8} \text{ s}^{-2})} \right], 10^{-2} \text{ m}^2 \text{ s}^{-1} \right\}. \quad (21)$$

The spatial distribution of geothermal heat fluxes  $Q_{\text{geo}}(x, y)$  ( $\text{W m}^{-2}$ ; Goutorbe et al. 2011) is depicted in

Fig. 2c. The flux  $Q_{\text{geo}}$  averages  $65.5 \text{ mW m}^{-2}$  in the ocean and represents a global energy flux of 23.7 TW. We note that this average heat supply is somewhat weaker than most earlier estimates (Stein and Stein 1992; Pollack et al. 1993; Huang 1999), which fall within  $80\text{--}100 \text{ mW m}^{-2}$ , possibly owing to a low bias in young oceanic crust (Goutorbe et al. 2011). Therefore, the presented transformation estimate by geothermal heating is likely to be a lower bound.

### 3. Preliminary remarks

The near-field mixing parameterization given by (19) and (20) aims at mimicking bottom-intensified mixing by breaking internal waves over rough topography (St. Laurent et al. 2002). The increase of energy dissipation with depth implied by (19) has some implications for the associated buoyancy forcing and circulation, as illustrated in Fig. 3a. Starting from the advective–diffusive balance of (2) and neglecting diapycnal variations of the thermal expansion and haline contraction coefficients (a rough but not unreasonable approximation in the deep

ocean, which has relatively weak  $\Theta$ ,  $S_A$  variations; see [appendix A](#)), the velocity induced by diapycnal mixing may be approximated by

$$\begin{aligned}\omega &= (\partial_{\perp}\rho)^{-1}\partial_{\perp}(K_{\perp}\partial_{\perp}\rho) \approx -\frac{1}{N^2}\partial_z(K_{\perp}N^2) \\ &= -\frac{1}{N^2}\partial_z(R_f\varepsilon_T).\end{aligned}\quad (22)$$

Since  $R_f\varepsilon_T$  decays away from the bottom,  $\omega > 0$  and mixing drives transport toward higher densities (which we will refer to as downwelling or downward transport for simplicity, although this transport is not necessarily vertical). Indeed, the downward buoyancy flux associated with upward-decaying  $\varepsilon_T$  is divergent, and the resultant increase in density must be compensated by downward advection across isopycnals. Yet, in the approximation of a linear equation of state and ignoring the geothermal heat source at the seabed, mixing can only redistribute buoyancy, and sinks and sources of buoyancy must balance each other. Because of the zero stratification of the bottom boundary layer and the no-flux bottom boundary condition, the downward buoyancy flux induced by diapycnal mixing  $K_{\perp}N^2$  must vanish at the seabed, implying a strong convergence of the buoyancy flux in the vicinity of the seafloor ([Ledwell et al. 2000](#); [St. Laurent et al. 2001](#); [Simmons et al. 2004](#); [Melet et al. 2013a](#)). When geothermal heating is taken into account, buoyancy convergence near the bottom is increased as the net downward diffusive buoyancy flux induced by mixing must eventually match an opposite sign, upward bottom buoyancy flux.

Thus, in the presence of geothermal heating and a bottom-intensified mixing energy according to (19) and (20), the bottommost waters gain buoyancy, whereas the overlying waters lose buoyancy. Note that increasing the vertical decay scale  $\zeta$  of energy dissipation will not modify the regions of buoyancy loss and buoyancy gain but will slightly reduce the buoyancy gain near the seabed and spread the compensating buoyancy loss higher in the water column. Rather than triggering convective instability, this buoyancy transfer is cancelled by diapycnal advection, with relatively weak but widespread downwelling away from the seabed and strong upwelling along topographic features ([Fig. 3a](#)). This behavior has been noted in observations of enhanced abyssal mixing near rough topography, such as in the Brazil basin ([Polzin et al. 1997](#); [Ledwell et al. 2000](#); [St. Laurent et al. 2001](#)). Note that the bottom layer that concentrates buoyancy deposition is characterized by a vanishing mixing efficiency, reconciling (19) and (22) with  $\omega < 0$  near the seafloor ([St. Laurent et al. 2001](#)).

An increase of internal wave energy dissipation with depth does not systematically characterize the deep

ocean (e.g., [Toole et al. 1994](#); [Waterhouse et al. 2014](#)). Indeed, observations of internal wave activity over smooth bathymetry generally show no significant bottom intensification of energy dissipation ([Toole et al. 1994](#); [Kunze and Sanford 1996](#); [Polzin et al. 1997](#)). The induced buoyancy flux may then decrease toward the seafloor, causing buoyancy gain and upwelling over a wider depth range away from the seabed ([Fig. 3b](#)). Yet, because of geothermal heating and the need for the diffusive buoyancy flux to vanish close to the seabed, waters banked along topographic slopes are likely to experience increased buoyancy gain relative to horizontally adjacent waters ([Fig. 3b](#)). This effect, related to hypsometry (the decrease of the ocean's horizontal area with depth), implies that upwelling may occur preferentially along the sloping topography even in the absence of enhanced wave breaking near the seafloor.

Several consequences may be drawn from the previous remarks. First, it can be hypothesized that global AABW consumption and upwelling occur primarily along the bottom topography. This hypothesis is consistent with suggestions that diabatic upwelling of dense waters is mostly confined to below the crests of the major topographic ridges ([Lumpkin and Speer 2007](#); [Huussen et al. 2012](#); [Ferrari et al. 2014](#)). A focused upwelling along topography implies in turn that the circulation induced by such mixing would be very different in a flat bottom ocean. Second, it can be expected that water masses covering the largest portions of the seabed will exhibit the strongest consumption rates or, to rephrase, that dianeutral upwelling will peak within the neutral density layer that has the largest incrop area. Indeed, two related effects combine to reinforce potential upwelling rates within density layers occupying a large seafloor area: increased exposure to near-bottom buoyancy deposition by abyssal mixing and geothermal heating and weak bottom diapycnal density gradients requiring strong velocities to balance the buoyancy gain.

The incrop area, defined by

$$\mathcal{J}(\gamma) = (1/\Delta\gamma) \iint_{I_{[\gamma-(\Delta\gamma/2), \gamma+(\Delta\gamma/2)]}} dA,$$

is plotted in [Fig. 4a](#). The term  $\mathcal{J}(\gamma)$  exhibits a maximum at  $\gamma = 28.20 \text{ kg m}^{-3}$  within the Southern Ocean (thick red line) and a much stronger peak at  $\gamma = 28.11 \text{ kg m}^{-3}$  within the 30°S–67°N region (thick blue line). Consequently, dianeutral upwelling north of 30°S may be expected to peak at  $\gamma = 28.11 \text{ kg m}^{-3}$ . In addition, mass conservation dictates that the surface of maximum dianeutral transport north of 30°S must correspond to the level of maximum cumulated northward dense water transport at 30°S, except for potential, small additional inflow of waters denser than  $28.11 \text{ kg m}^{-3}$  from the north (see [Figs. 5a,b](#); [Ganachaud and Wunsch 2000](#)). In

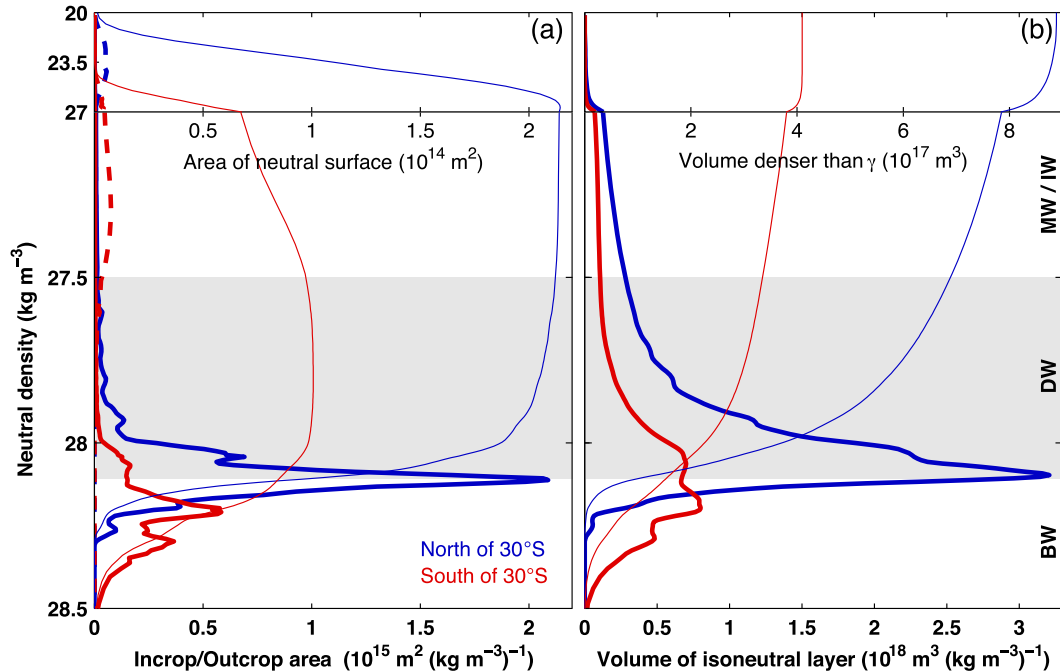


FIG. 4. Key characteristics of the climatological neutral density field, for ocean domains north (blue) and south (red) of 30°S. (a) Incrop (thick lines), outcrop (thick dashed lines), and neutral surface (thin lines) areas as a function of neutral density  $\gamma$ . (b) Isoneutral layer volume (thick lines) and volume of waters denser than  $\gamma$  (thin lines) as a function of neutral density  $\gamma$ . Note the different vertical scale above and below  $\gamma = 27 \text{ kg m}^{-3}$  and the upper x axis for thin lines. Neutral density ranges of bottom water (BW), deep water (DW), and mode/intermediate water (MW/IW) are indicated by the light gray shading and the right-side labels.

other words, if dianeutral transport north of 30°S peaks at  $28.11 \text{ kg m}^{-3}$ , then the overturning streamfunction at 30°S should also peak near  $28.11 \text{ kg m}^{-3}$ . Indeed, the  $28.11 \text{ kg m}^{-3}$  neutral surface is the approximate boundary between northward abyssal flow and southward deep-water flow at 30°S found by inverse studies (Ganachaud and Wunsch 2000; Lumpkin and Speer 2007), supporting our inference from the climatological density field. Defining the light end of AABW as the neutral density level at which the abyssal overturning streamfunction peaks, we will thus refer to AABW as waters characterized by  $\gamma \geq 28.11 \text{ kg m}^{-3}$ .

A closer look at the latitudinal structure of the incrop area (Fig. 5a) reveals that  $\sim 28.11 \text{ kg m}^{-3}$  waters are in contact with the seafloor mostly in the Northern Hemisphere and that the maximum incrop area gradually moves toward lighter densities from south to north. (In Fig. 5a, the density-binned values of incrop area are reprojected to pseudodepth for visual purposes. The remapping procedure involves a simple bottom-up filling of each latitude band with ocean grid cells ordered from dense to light.) This supports the idea that the densest abyssal waters that cover the seafloor are gradually converted to lighter densities as they move northward. Preferential consumption of bottommost

waters leads to progressive homogenization of AABW, reducing the abyssal stratification and thereby increasing the thickness and incrop area of the dominant neutral density layers (Figs. 4, 5). This in turn reinforces the efficiency of AABW consumption near the seabed, allowing potentially strong diabatic transport across the  $28.11 \text{ kg m}^{-3}$  neutral surface in northern basins.

#### 4. Water mass transformation estimates

##### a. Transformation by near-field mixing and geothermal heating

###### 1) LOCAL DIANEUTRAL TRANSPORTS

The spatial structure of dianeutral transports induced by locally dissipating internal tides, lee waves, and geothermal heating is illustrated in Figs. 6 and 7. Local dianeutral transports forced by mixing dominate those forced by geothermal heat fluxes (Fig. 6). Because lee-wave generation occurs mainly along the deep Southern Ocean floor, lee-wave-driven transformation appears dominated by a dipole of lightening below  $28.15 \text{ kg m}^{-3}$  and densification above. Internal tides are generated at various depths and densities, resulting in a more noisy

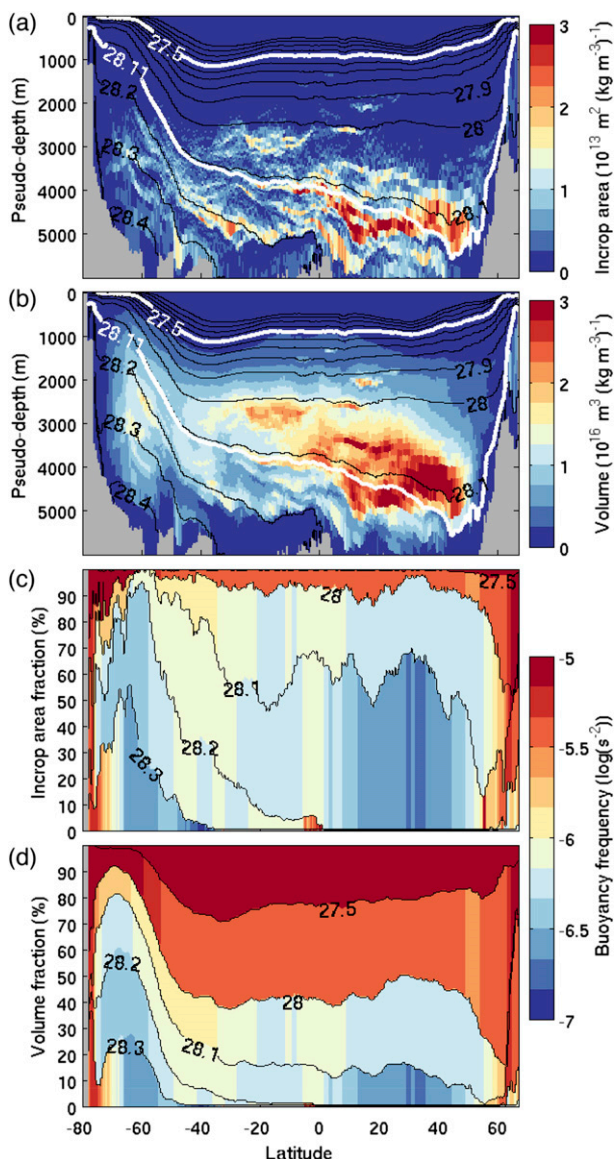


FIG. 5. (top) Along-isopycnal zonal sum of (a) incrop area and (b) isoneutral layer volume, where the density-binned values are reprojected to pseudodepth for visual purposes. The remapping procedure involves a simple bottom-up filling of each latitude band with ocean grid cells ordered from dense to light. Note that we use a variable density step  $\Delta\gamma$  for appropriate sampling. (c),(d) Fraction of (c) seabed area and (d) ocean volume occupied by six neutral density layers and their volume-averaged stratification (shading) as a function of latitude, illustrating the gradual lightening and homogenization of AABW as it progresses northward. The Arctic Ocean and marginal seas are excluded from all calculations.

distribution of positive and negative transports. Whereas mixing transfers buoyancy across isoneutral layers, the geothermal heat flux causes only lightening and upward transport. In addition, the spatial pattern of the induced geothermal transports resembles closely that of the incrop area shown in Fig. 5a: geothermal heating consumes most

efficiently water masses blanketing vast seafloor areas, so that dianeutral transports appear aligned along the  $28.11 \text{ kg m}^{-3}$  surface.

Figure 7 shows the horizontal pattern of upwelling and downwelling across specific neutral surfaces, chosen as the neutral density level of maximum net upwelling globally. Unsurprisingly, the level of maximum upwelling due to lee-wave breaking coincides with the peak incrop area south of  $30^\circ\text{S}$  ( $\gamma = 28.20 \text{ kg m}^{-3}$ ), while peak upwelling rates due to near-field tidal mixing and geothermal heating coincide with the peak incrop area north of  $30^\circ\text{S}$  ( $\gamma = 28.11 \text{ kg m}^{-3}$ ). Mixing driven by internal tides and lee waves results in downwelling across wide areas, including strong downwelling where the surface approaches the seafloor but upwelling where the neutral surface grounds. Geothermal heating acts only where the neutral density layer (of thickness  $\Delta\gamma$ ) covers the ocean floor (Fig. 7c), which is also the area where near-field mixing causes upwelling (Fig. 7a). Upwelling across the  $28.11 \text{ kg m}^{-3}$  surface by geothermal heating and tidal mixing is concentrated on the sides of major oceanic ridges and along topographic slopes of the North Pacific.

## 2) TOTAL DIANEUTRAL TRANSPORTS

The water mass transformation rate as a function of neutral density is obtained by summing the local dianeutral transports over neutral surfaces (Fig. 8). The volume rate of water mass formation or consumption in a given density class  $[\gamma_1, \gamma_2]$  corresponds to the difference in transformation rates  $T(\gamma_2) - T(\gamma_1)$ . Any volume loss within one density class must be balanced by a volume gain in another density class.

Internal tides, lee waves, and geothermal heating have qualitatively different impacts on water mass transformation (Fig. 8a). Whereas geothermal heat fluxes induce only negative rates (buoyancy gain), diapycnal mixing must extract buoyancy from one water mass in order to supply buoyancy to another. This behavior is most clearly apparent in the lee-wave transformation curve, which exhibits a dipole of positive and negative transports: lee-wave-driven mixing is a net source (sink) of buoyancy for waters denser (lighter) than  $28.15 \text{ kg m}^{-3}$ . This results in the formation of 9 Sv of  $28.05\text{--}28.20 \text{ kg m}^{-3}$  waters, at the expense of denser and lighter water masses, which together lose volume at the same rate. In the case of baroclinic tides, buoyancy gain (upwelling) dominates for neutral densities greater than  $27.20 \text{ kg m}^{-3}$ , while buoyancy loss prevails for lighter waters. Indeed, the total downward buoyancy flux associated with near-field tidal mixing is convergent over most of the deep-ocean density range (Fig. 9a). In contrast, the buoyancy flux due to dissipating lee waves

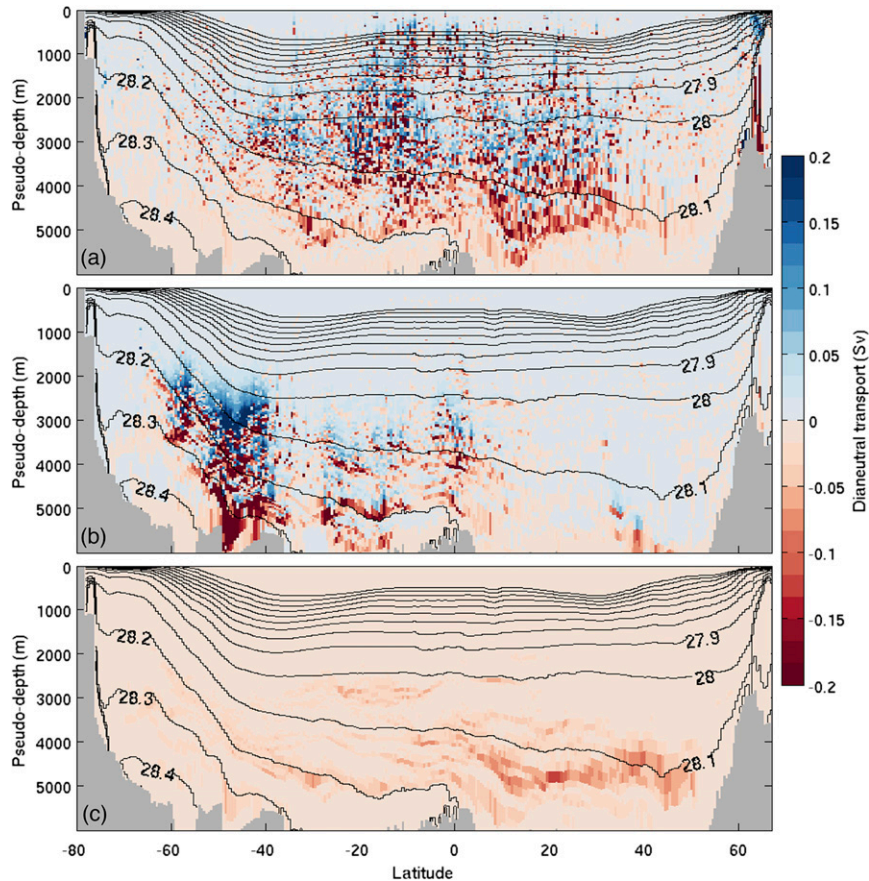


FIG. 6. Along-isopycnal zonal sum of dianeutral transports (Sv) induced by locally dissipating (a) internal tides and (b) lee waves and by (c) geothermal heating, where the density-binned values are reprojected to pseudodepth for visual purposes. Shaded cells depict the rate of upwelling (red) or downwelling (blue) within each neutral density layer and each latitude band.

peaks at  $28.15 \text{ kg m}^{-3}$ , well within the AABW layer (Fig. 9b).

Parameterized near-field tidal mixing drives  $\sim 9 \text{ Sv}$  of upwelling across the  $28.11 \text{ kg m}^{-3}$  surface globally, of which  $2 \text{ Sv}$  are attributable to internal tides generated by abyssal hill roughness (Fig. 8a). Despite the relatively weak local transports due to geothermal heating (Figs. 6 and 7), its peak transformation rate of  $-5.5 \text{ Sv}$  at  $\gamma = 28.11 \text{ kg m}^{-3}$  is of comparable magnitude to the maximum upwelling rate due to locally dissipating internal tides. On the other hand, parameterized mixing from breaking lee waves results in net downwelling across the  $28.11 \text{ kg m}^{-3}$  surface, consuming about  $6 \text{ Sv}$  of waters denser than  $28.20 \text{ kg m}^{-3}$  but forming about  $7 \text{ Sv}$  of lighter AABW. Decomposing dianeutral transports between the Southern Ocean ( $80^\circ\text{S}$ – $30^\circ\text{S}$ ; Fig. 8c) and other basins ( $30^\circ\text{S}$ – $67^\circ\text{N}$ ; Fig. 8b) reveals that water mass transformation is dominated by tidal mixing and geothermal heating north of  $30^\circ\text{S}$  and by lee-wave-driven mixing south of  $30^\circ\text{S}$ . North of  $30^\circ\text{S}$ , tidal mixing and

geothermal heating consume, respectively, about  $8$  and  $5 \text{ Sv}$  of AABW, whereas upwelling forced by lee waves remains weaker than  $2 \text{ Sv}$ , a contribution similar to that of internal tides generated by abyssal hills. Lee-wave-driven mixing is concentrated in the Antarctic Circumpolar Current (ACC), where it converts  $\sim 5 \text{ Sv}$  of bottom waters heavier than  $28.3 \text{ kg m}^{-3}$  into lighter AABW and draws  $\sim 3 \text{ Sv}$  of lighter, deep waters into the AABW density range. Hence, according to the present parameterization, mixing by breaking lee waves is little involved in the diabatic return of AABW flowing out of the Southern Ocean. Rather, it participates in the lightening of the densest AABW, while enhancing bottom-water flow by forming additional, lighter AABW prior to its escape into the Atlantic and Indo-Pacific basins.

The shape of the geothermal transformation and its narrow peak at  $28.11 \text{ kg m}^{-3}$  are not controlled by spatial contrasts in heat fluxes (Fig. 2c) but rather by the incrop area (Fig. 4a), as postulated in section 3 (see

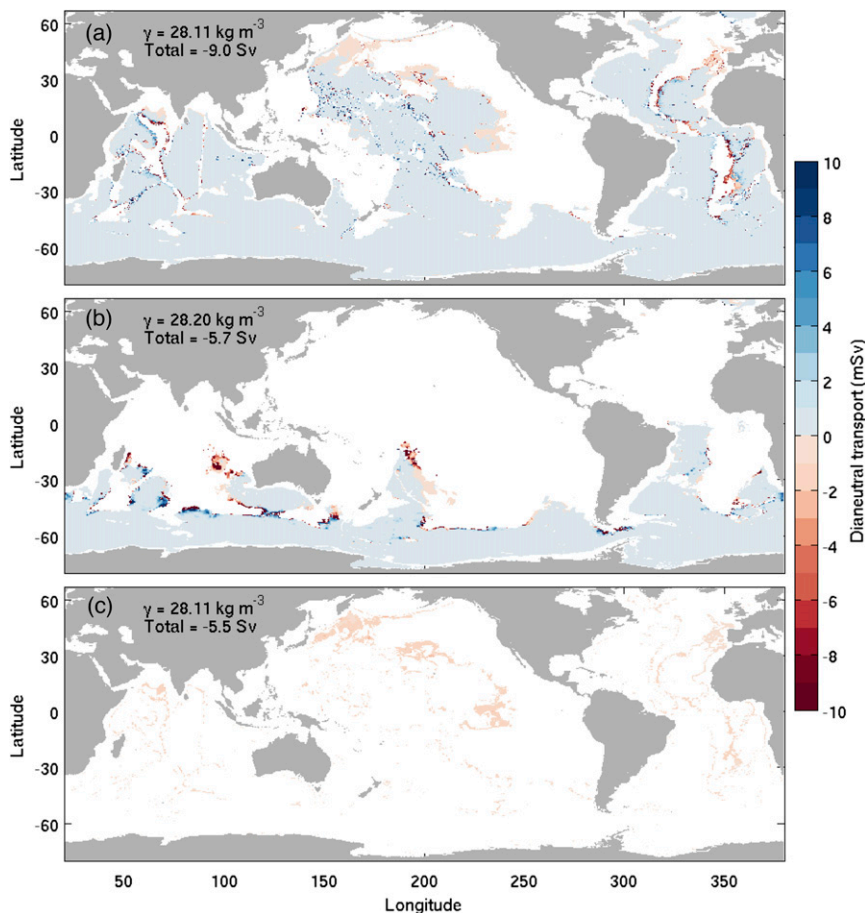


FIG. 7. Maps of dianeutral transport (mSv) induced by locally dissipating (a) internal tides and (b) lee waves and by (c) geothermal heating across neutral surfaces  $\gamma = 28.11$ ,  $28.20$ , and  $28.11 \text{ kg m}^{-3}$ , respectively. These neutral surfaces correspond to the respective density levels of maximum global upwelling. Mixing causes dianeutral transports toward both lighter (red) and denser (blue) water. Geothermal heating causes dianeutral transport toward lighter waters within the bottommost neutral density layer ( $\Delta\gamma = 0.005 \text{ kg m}^{-3}$  at  $\gamma = 28.11 \text{ kg m}^{-3}$ ).

appendix B for further discussion). Similarly, the sharp decrease of the area of neutral surfaces at  $28.11 \text{ kg m}^{-3}$  (Fig. 4a), equivalent to the sharp peak of the incrop area, controls the peak tidal transformation by forcing a strong convergence of the total buoyancy flux near  $28.11 \text{ kg m}^{-3}$  (Fig. 9a). Hence, the concomitant maxima of geothermal and tidal transformations, and their correspondence with the approximate boundary between deep and bottom waters, must not be seen as fortuitous. Rather, a dynamic–thermodynamic equilibrium is reached in which AABW is gradually transformed into densities close to  $28.11 \text{ kg m}^{-3}$  as it progresses through the Southern Ocean and farther northward along the sea bottom, so that a voluminous, weakly stratified water mass occupies a vast portion of the World Ocean floor and maximizes its exposure to geothermal heating and abyssal mixing (Figs. 4, 5).

### 3) SENSITIVITY TO THE VERTICAL DECAY SCALE $\zeta$

The overall efficiency of mixing energy in supplying buoyancy to the deep ocean depends on its distribution relative to the neutral density field and in particular on the degree of cancellation between convergent and divergent buoyancy fluxes. Parameterized near-field tidal mixing drives a net source of buoyancy over most of the ocean interior, fluxing buoyancy from the upper ocean down to deep and abyssal waters (Fig. 9a). On the other hand, because the energy of dissipating lee waves is placed at large depths (90% of the estimated lee-wave generation occurs below 3000 m), the resultant mixing is unable to bring heat from thermocline waters to the deep ocean (Fig. 9b). Nevertheless, the efficiency of buoyancy transfer from light to dense waters may be enhanced if the vertical decay scale  $\zeta$  is increased, that is,

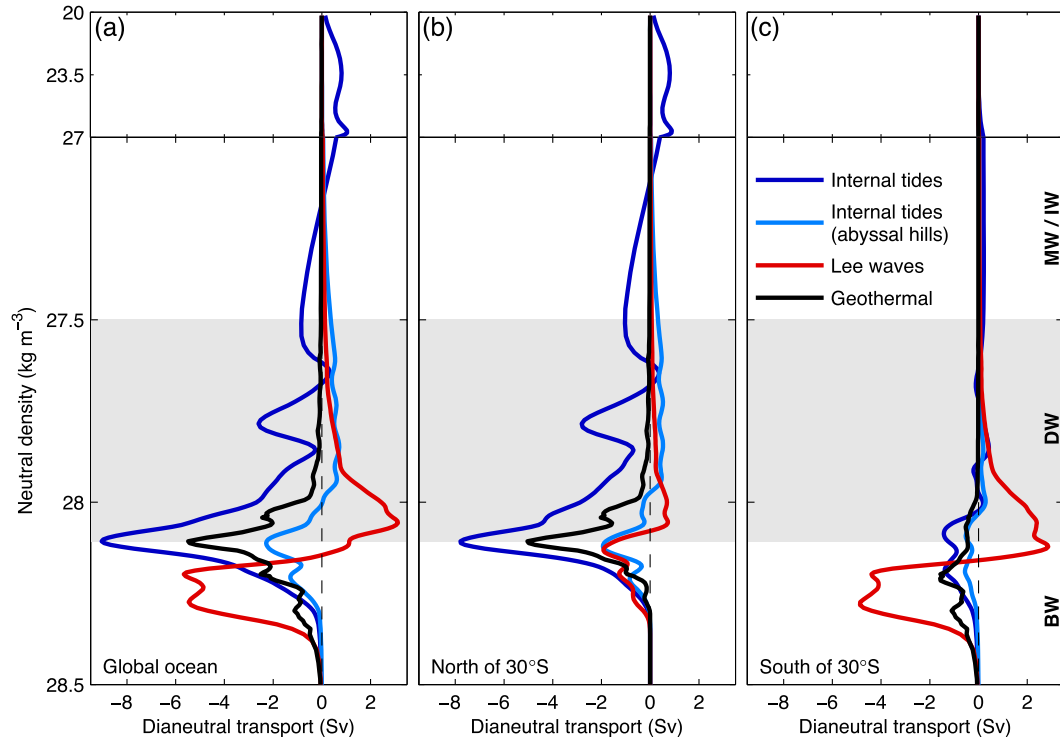


FIG. 8. Water mass transformation by near-field diapycnal mixing and geothermal heating. (a) Global, (b) 30°S–67°N, and (c) 80°–30°S dianeutral transports resulting from geothermal heating (black) and from near-field mixing by internal tides (blue), internal tides generated by abyssal hills only (pale blue), and lee waves (red). To minimize data noise resulting from the patchiness of mixing and induced transports (see Figs. 6 and 7), the transformation profiles shown are obtained using (17) and (18), where a small degree of smoothing is applied to the total buoyancy flux before taking the  $\gamma$  derivative. Note the different vertical scale above and below  $\gamma = 27 \text{ kg m}^{-3}$ . Neutral density ranges of BW, DW, and MW/IW waters are indicated by the light gray shading and the right-end labels.

if internal wave energy tends to dissipate higher in the water column.

Figure 9 illustrates the sensitivity of transformation estimates to the  $\zeta$  parameter. Different  $\zeta$  values result in weak overall differences in buoyancy fluxes and dianeutral transports. A doubling of the decay scale increases the tidally driven buoyancy flux out of the thermocline and into the deep ocean, resulting in slightly greater upwelling rates within the 27–28.1  $\text{kg m}^{-3}$  density range but virtually unchanged transformation within the AABW layer (Figs. 9a,d). Doubling  $\zeta$  also slightly smoothens and shifts upward the peak buoyancy flux driven by lee waves, reducing downwelling across the deep/bottom-water boundary but leaving the transformation estimate largely unchanged (Figs. 9b,e). On the other hand, reducing the decay scale to 300 m tends to accentuate somewhat peak dianeutral transports, including a 1 Sv increase of tidally driven AABW consumption due to an increased buoyancy flux across  $\gamma = 28.11 \text{ kg m}^{-3}$  but deviations from the reference curve remain no greater than 2 Sv (Figs. 9a–f).

Hence, in our climatological setting, water mass transformation by near-field mixing is not set by the choice of vertical decay scale for energy dissipation but more so by the ocean's density structure and bathymetry, combined with the horizontal distribution of internal wave generation. While demonstrating the robustness of the present transformation estimates, this weak sensitivity contrasts with results from OGCM experiments showing enhanced abyssal flow under larger  $\zeta$  (Saenko et al. 2012; Oka and Niwa 2013). The difference could arise from the response of stratification to mixing in numerical experiments: strong, focused, near-bottom mixing may weaken the simulated local stratification and ultimately reduce its ability to sustain a buoyancy flux.

#### b. Transformation rates due to far-field mixing

##### 1) ENERGY DISTRIBUTION FOR REMOTE DISSIPATION

In the preceding subsection, we have examined transformation rates associated with the commonly used

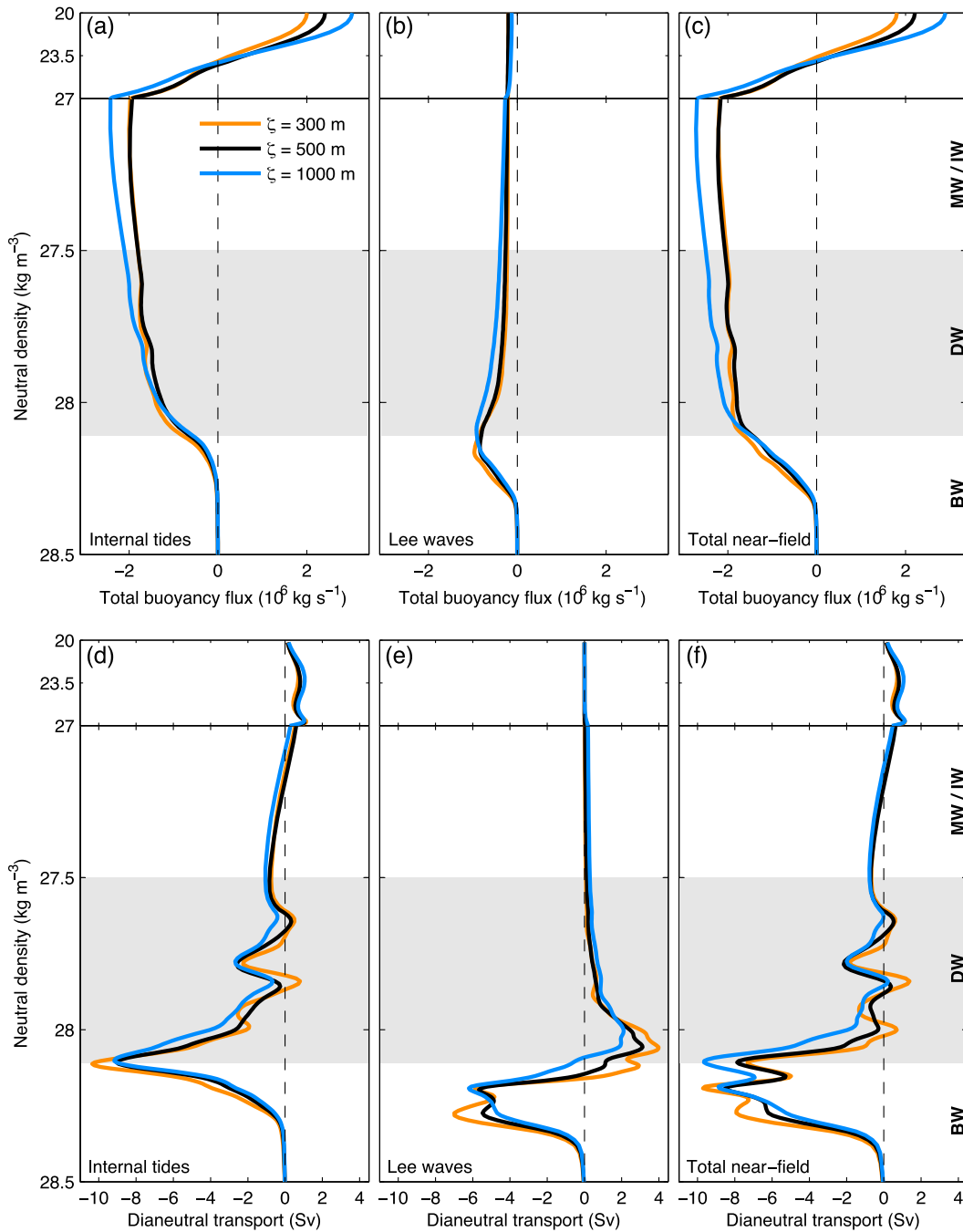


FIG. 9. Sensitivity of global water mass transformation by near-field mixing to the vertical decay scale of energy dissipation. Shown are (top) neutral density fluxes and (bottom) dianeutral transports induced by locally dissipating (a),(d) internal tides, (b),(e) lee waves, and (c),(f) both, using an  $e$ -folding length  $\zeta$  of 300 (orange), 500 (black), and 1000 m (pale blue) in the vertical structure function of (19). Black curves correspond to the reference case shown in previous figures.

mixing parameterization for internal waves that dissipate near their generation sites. Because less is known about the dissipation of internal waves than about their generation, it is assumed that one-third of the wave

energy dissipates where it is generated, while the other two-thirds are ignored or assumed to contribute to sustain a background vertical diffusivity of about  $10^{-5} \text{ m}^2 \text{ s}^{-1}$  (St. Laurent et al. 2002; Simmons et al.

2004). Yet, using a map of the depth-integrated tidal energy dissipation diagnosed from global numerical simulations (Niwa and Hibiya 2011), Oka and Niwa (2013) recently extended the parameterization to include far-field tidal mixing. To specify the vertical structure of energy dissipation, the authors used an exponential decay from the bottom for the fraction  $q$  of locally dissipating energy but assumed a vertically uniform  $\varepsilon_T$  for remote dissipation.

To explore the implications of various assumptions about the distribution of far-field mixing energy, we calculate transformation rates due to remotely dissipating internal tides under various idealized scenarios. We construct two scenarios for the horizontal distributions of the energy flux  $E_{\text{far-field}}(x, y)$  ( $\text{W m}^{-2}$ ):

- (Su) uniformly distributed energy over the whole ocean volume, where  $E_{\text{far-field}}(x, y)$  is proportional to local water depth  $H(x, y)$ ; and
- (Sp) the horizontal spread of energy around generation sites, where  $E_{\text{far-field}}(x, y)$  is obtained by uniformly redistributing the energy flux  $(1 - q_{\text{IT}})E_{\text{IT}}(x, y) + (1 - q_{\text{ITAH}})E_{\text{ITAH}}(x, y)$  within a radius of 1000 km of each  $(x, y)$  grid point. This ad hoc procedure aims at grossly mimicking horizontal propagation of internal tide energy, as observed in maps produced by Niwa and Hibiya (2011).

Of particular interest for abyssal water mass transformation is the fraction of far-field energy dissipated in shallow versus deep areas of ocean basins. The percentage of mixing energy located in ocean areas deeper than 3000 m is 92% under scenario Su, dropping to 67% in scenario Sp. For comparison, the percentage of local tidal dissipation occurring within the same area is 30%. Both scenarios thus imply that far-field dissipation contributes more energy to deep oceanic regions than near-field dissipation, possibly departing from real conditions if most of the remote tidal dissipation was to occur at continental shelves and upper continental slopes (see, e.g., Nash et al. 2004; Martini et al. 2011; Kelly et al. 2013; Waterhouse et al. 2014). Nonetheless, the two distributions are sufficiently different that they should hint at the sensitivity to the fraction of remote dissipation taking place in shallow waters.

The vertical structure of energy dissipation is specified according to the following scenarios:

- (S2)  $\varepsilon_T$  proportional to  $N^2$ , that is, constant  $K_{\perp}$ ;
- (S1)  $\varepsilon_T$  proportional to  $N$ , that is,  $K_{\perp}$  proportional to  $N^{-1}$ ;
- (S0) constant  $\varepsilon_T$ , that is,  $K_{\perp}$  proportional to  $N^{-2}$ ; and
- (S-1)  $\varepsilon_T$  proportional to  $N^{-1}$ , that is,  $K_{\perp}$  proportional to  $N^{-3}$ .

The numbering of the scenarios corresponds to exponents of  $N$  in the assumed dependence of dissipation to stratification. Scenario S2 is believed to be typical of nonlinear energy transfer and dissipation in a uniform internal wave field described by a Garrett–Munk spectrum (Garrett and Munk 1972; Müller et al. 1986) and was the form used by Koch-Larrouy et al. (2007). Scenario S1 corresponds to the vertical structure suggested by Gargett (1984) and subsequently used in ocean modeling (Cummins et al. 1990). Scenario S0 was used in simulations of Oka and Niwa (2013). Scenario S-1 is the only scenario for which the far-field energy dissipation increases with depth.

By combining the proposed horizontal and vertical distributions, we obtain eight scenarios with identical overall power available for mixing, equal to 0.85 TW. Scenario S2u (the combination of Su and S2) results in a globally uniform eddy diffusivity of  $1.23 \times 10^{-5} \text{ m}^2 \text{ s}^{-1}$ . We stress here that these scenarios are not meant to provide realistic parameterizations of far-field tidal mixing nor to span all possible outcomes for the energy of low-mode internal tides. Rather, they are meant to achieve preliminary understanding and to explore the sensitivity to key choices in constructing the energy distribution.

## 2) DIANEUTRAL TRANSPORTS

The resulting transformation curves are shown in Fig. 10. The differing horizontal distributions across scenarios Su (upper panels) and Sp (lower panels) have a relatively modest impact on water mass transformation north of 30°S (Figs. 10b,e). Significant qualitative differences appear only in the Southern Ocean, where the weak internal tide generation results in negligible mixing under scenario Sp but in significant mixing under Su (Figs. 10c,f). Yet, even under Su, Southern Ocean dianeutral transports induced by far-field tidal mixing remain quite weak overall, with peak upwelling rates not exceeding 6 Sv. Except under scenario S1u, for which far-field mixing drives 4 Sv of AABW consumption south of 30°S, AABW transformation in the Southern Ocean is dominated by the parameterized lee-wave dissipation. The weak Southern Ocean transports relative to those occurring north of 30°S can be largely explained by the stronger stratification of the Southern Ocean abyss and the associated lack of large incrop areas. In the following, we refer exclusively to dianeutral transports for the 30°S–67°N region (Figs. 10b,e).

North of 30°S, peak transformation rates tend to be enhanced under the uniform volume distribution Su compared with the horizontally spread distribution Sp, as might be expected from the former's greater power availability in the open ocean and over abyssal plains in particular. The transformation estimates remain qualitatively similar,

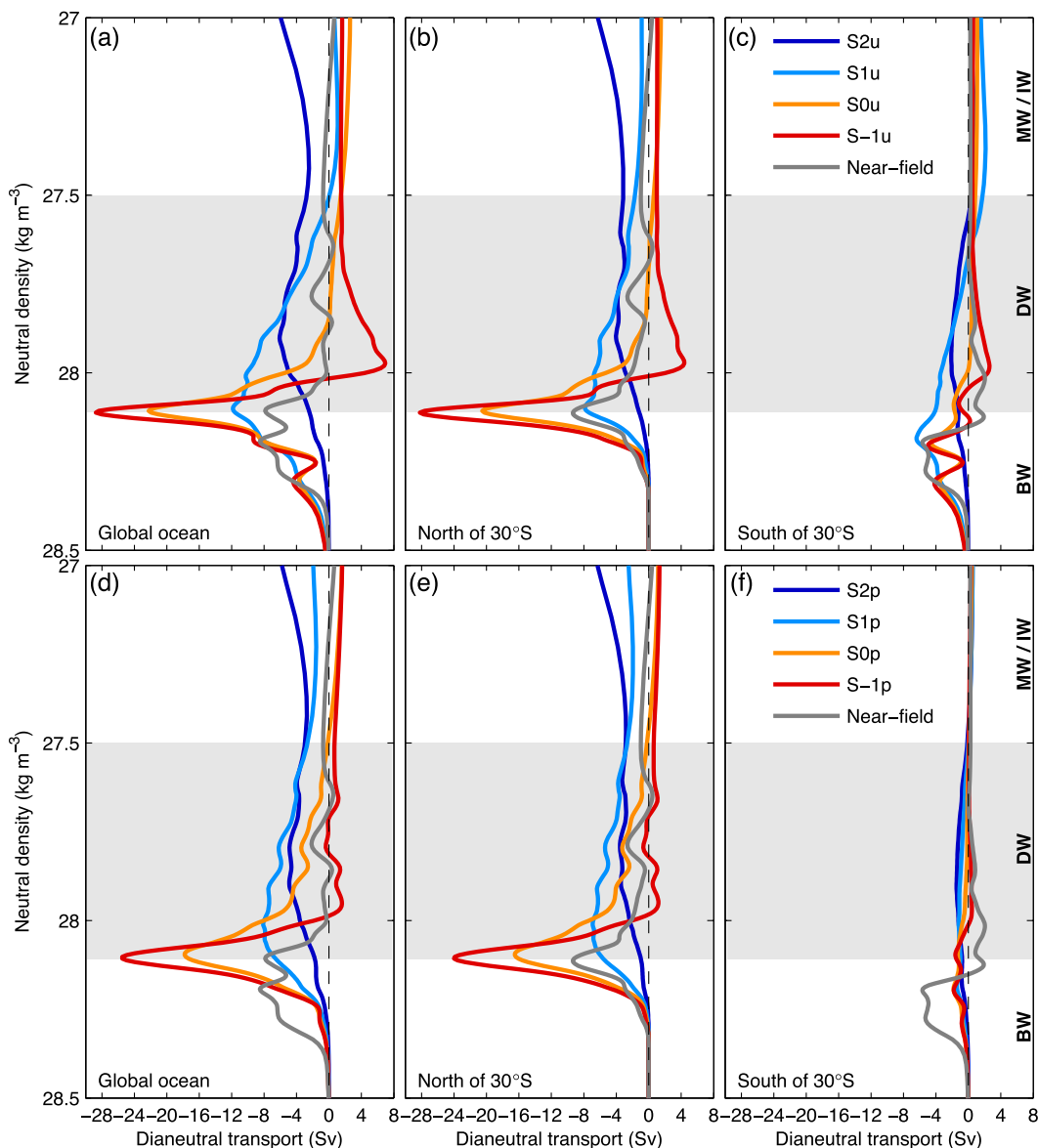


FIG. 10. Water mass transformation by far-field tidal mixing under eight idealized scenarios for (a),(d) global, (b),(e) 30°S–67°N, and (c),(f) 80°–30°S ocean domains. The horizontal energy distribution is specified according to assumption (top)  $S_u$  or (bottom)  $S_p$  and the vertical energy structure scales either as  $N^2$  (S2, blue),  $N$  (S1, pale blue), 1 (S0, orange), or  $1/N$  (S-1, red). Transformation by near-field mixing (both lee waves and internal tides) is plotted in gray for comparison.

however, suggesting that the details of the horizontal distribution of the open-ocean dissipation are not crucial to the large-scale water mass conversion. In contrast, Dianeutral transports forced by parameterized far-field mixing are strongly sensitive to the vertical structure given to energy dissipation.

The uniform diffusivity of scenario S2 results in  $\sim 3$  Sv of upwelling within deep-water masses, but the upwelling rate drops to only 1 Sv at the deep/bottom-water boundary, implying negligible AABW consumption. Under

scenario S1, a maximum Dianeutral transport of  $-7$  to  $-8$  Sv appears at or near the  $28.11 \text{ kg m}^{-3}$  neutral density level, with gradually decreasing upwelling toward lighter and denser waters. Thus, under the assumption that remote dissipation scales as  $N$ , far-field mixing could balance a significant portion of the estimated northward abyssal flow at 30°S.

The vertically homogenous energy dissipation rate of scenario S0 has radically different implications for the overturning circulation. Indeed, aside from effects

associated with the nonlinearity of the equation of state (see [appendix A](#) for a discussion of these effects), a vertically uniform buoyancy flux implies that convergence occurs only at the seafloor, with no impact on the remainder of the water column except for compensating divergence at the surface. Thus, under such mixing, buoyancy is extracted at the base of the mixed layer and fluxed directly to the bottom boundary layer, with nonlinearity in the equation of state contributing some additional buoyancy loss in upper waters and some additional buoyancy gain at depths ([appendix A](#)). Consequently, the resultant water mass transformation displays a shape quite similar to that associated with geothermal heating, with upwelling reaching a maximum of 16–21 Sv at the boundary between deep and abyssal waters. Hence, given a constant mixing efficiency of one-sixth, 0.85 TW of uniformly distributed energy dissipation may provide for  $\sim 20$  Sv of bottom-water consumption.

Even stronger AABW consumption can be obtained by applying a vertical profile of wave-breaking energy proportional to  $1/N$  as assumed in scenario S-1. Here, efficient lightening of abyssal waters is achieved at the expense of waters lighter than  $28 \text{ kg m}^{-3}$ , most of which undergo densification. Dianeutral transport across  $\gamma = 28.11 \text{ kg m}^{-3}$  reaches  $-23 \text{ Sv}$  in S-1p and  $-28 \text{ Sv}$  in S-1u. This scenario highlights the result that rates of deep-water mass conversion and the implied ocean circulation do not depend as much on the overall consumed power as they do on the spatial—and especially vertical—distribution of energy lost to the internal wave field.

In summary, by carrying energy away from major topographic features toward deeper parts of ocean basins, low-mode internal tides could be more efficient than their locally dissipating counterpart in supplying buoyancy to bottom water masses. However, the actual impact of low-mode internal tides on AABW consumption depends on the (largely unknown) location of their ultimate decay into small-scale turbulence. Results from the tested idealized scenarios suggest that the fraction of remote dissipation occurring in the open ocean and the vertical structure of the open-ocean dissipation are key uncertainties in the far-field energy distribution. Insignificant AABW consumption is to be expected if remote dissipation occurs primarily at continental margins or within the pycnocline, whereas a leading role of far-field tidal mixing in consuming AABW is possible if the associated mixing energy is more evenly distributed over the ocean's volume.

## 5. Relation with previous studies

### a. Diapycnal mixing

The present transformation estimate due to near-field mixing is consistent with previous OGCM studies but

inconsistent with the analogous estimate of [Nikurashin and Ferrari \(2013\)](#). We show that, excluding the added contribution of abyssal hill roughness, parameterized tidal mixing according to (19) and (21) drives the upwelling of 6 Sv of bottom waters north of  $30^\circ\text{S}$ , in broad agreement with a  $\sim 5$ -Sv enhancement of the lower branch of the overturning circulation in numerical experiments ([Saenko and Merryfield 2005](#)). [Melet et al. \(2014\)](#) show that including lee-wave radiation as a second source of mixing slightly strengthens the abyssal overturning and shifts it toward lower densities, a response that closely matches our results. In contrast, [Nikurashin and Ferrari \(2013\)](#) estimated that the local dissipation of baroclinic tide and lee-wave energy drives 16 and 9 Sv of global AABW upwelling, respectively. The discrepancy with the present estimate comes from the contribution of the bottom layer of buoyancy gain. Their calculation excluded the near-bottom convergence of the buoyancy flux so that their values reflect the global diabatic sinking rates of interior waters in response to the divergent buoyancy flux associated with depth-increasing dissipation ([R. Ferrari and M. Nikurashin 2014](#), personal communication). Problematically, they seemed to imply that their estimates of interior transformation pertained to the upwelling rather than the downwelling of water masses. Our results are consistent with theirs for the interior transformation, but we find that the bottom layer contribution is as large and needs to be considered to compute the overall transformation rates. In particular, their estimate implied that both sources of mixing force net upwelling throughout the  $27\text{--}28.5 \text{ kg m}^{-3}$  neutral density range, whereas mixing due to breaking lee waves is expected to cause both negative and positive rates of transformation within this density range ([Fig. 8](#)). Given that other sources of mixing and buoyancy may contribute to AABW consumption, such as low-mode internal tides, geothermal heating, deep overflow mixing, or alternate dissipation routes of balanced flows, their values might also have appeared uncomfortably high.

Our idealized estimates of water mass transformation by far-field mixing shed light on the recent findings of [Oka and Niwa \(2013\)](#), who report a doubling of the simulated strength of the Pacific overturning circulation with the addition of vertically uniform dissipation for remotely breaking internal tides. It is shown that this assumption, a priori most simple, results in almost exclusive consumption of waters covering the seafloor, causing strong diabatic upwelling within the voluminous, weakly stratified water mass that occupies most of the seabed area of northern basins.

### b. Geothermal heating

The role of geothermal heating in converting abyssal waters has been quantified in a manner consistent with that of diapycnal mixing and is shown to be non-negligible. This agrees with a previous water mass transformation estimate (Emile-Geay and Madec 2009) and with earlier numerical studies reporting a significant geothermal influence on the lower overturning cell and North Pacific abyssal temperatures (Adcroft et al. 2001; Hofmann and Morales Maqueda 2009; Emile-Geay and Madec 2009). Despite relatively weak local buoyancy fluxes, geothermal heating efficiently consumes the thick, homogenous water mass that covers large seafloor areas of the North Pacific and eastern Atlantic (Fig. 7c). With about 5 Sv of induced AABW upwelling across the  $28.11 \text{ kg m}^{-3}$  neutral surface north of  $30^\circ\text{S}$ , geothermal heating almost rivals parameterized near-field tidal mixing in maintaining the northward AABW flow out of the Southern Ocean. This result suggests that geothermal heat fluxes have a nonnegligible part in the energy flows that sustain the abyssal overturning. The respective roles of diapycnal mixing and geothermal heating for ocean energetics can be compared by calculating their potential energy supply to the global ocean (e.g., Huang 1999; Nycander et al. 2007):

$$\partial_t E_p = g \iiint \partial_t \rho z dV, \quad (23)$$

$$(\partial_t E_p)_{\text{geo}} = g \iint_{I(0,+\infty)} \left( \frac{-Q_{\text{geo}} \alpha}{c_p^0} \right) (-H) dA, \quad \text{and} \quad (24)$$

$$(\partial_t E_p)_{\text{mix}} = g \iiint [\partial_\Theta \rho \partial_\perp F^\Theta + \partial_{S_A} \rho \partial_\perp F^{S_A}] z dV, \quad (25)$$

where no-flux surface and bottom boundary conditions must be applied in (25), as required for interior mixing alone. Equating  $\partial_\perp$  with  $-\partial_z$  and integrating by parts, (25) may be rewritten as

$$(\partial_t E_p)_{\text{mix}} = \iiint \rho K_\perp N^2 dV + g \iiint [F^\Theta \partial_z (\partial_\Theta \rho) + F^{S_A} \partial_z (\partial_{S_A} \rho)] z dV,$$

showing that  $(\partial_t E_p)_{\text{mix}}$  differs from  $\iiint \rho K_\perp N^2 dV = \iiint \rho R_f \varepsilon_T dV$  when accounting for spatial variations in  $\partial_\Theta \rho$  and  $\partial_{S_A} \rho$ .

Near-field mixing parameterized by (19) and (21) supplies potential energy at a total rate of 97 GW, with internal tides and lee waves contributing 64 and 33 GW, respectively. The geothermal contribution is of comparable magnitude, amounting to 35 GW. Geothermal heating efficiently raises the ocean's center of mass by

supplying buoyancy directly to the ocean bottom. On the other hand, of the 600 GW of internal wave energy assumed to be lost near generation sites, only 16.2% is ultimately converted to potential energy. This percentage, though close to  $R_f = 1/6$  in the present case, needs not be equal to the assumed mixing efficiency because of nonlinearity in the equation of state (which contributes  $-5$  and  $+9$  GW in the potential energy supply by internal tides and lee waves, respectively) and because of the upper-bound imposed on vertical diffusivity (which induces a net total loss of 7 GW). Note that the  $1 - R_f$  fraction of lee-wave and internal tide energy that dissipates through viscosity represents a quasi-negligible heat source for the ocean, with a total heat supply of 1.45 TW comparing to 23.7 TW of geothermal input globally.

## 6. Conclusions

A hydrographic climatology and estimates of available power from lee and tidally generated internal waves and from geothermal heating have been used to quantify rates of water mass transformation in the ocean interior. It was shown that parameterized near-field mixing under typical assumptions cannot account for the full strength of the abyssal overturning. The specified local dissipation of internal tide energy consumes about 8 Sv of AABW north of  $30^\circ\text{S}$ . Breaking lee waves, most energetic in the Southern Ocean, instead precondition abyssal waters prior to their escape north of the ACC, reducing their density but increasing their northward volume transport. In addition, geothermal heating, estimated to sustain about 5 Sv of AABW flow, was found to be a significant component of the abyssal overturning.

High mixing rates observed or inferred to prevail in the deep Southern Ocean (Oibers and Wenzel 1989; Heywood et al. 2002; Naveira Garabato et al. 2004; Sloyan 2005; Kunze et al. 2006) are often suggested to contribute prominently to the diabatic closure of the abyssal overturning circulation (Ito and Marshall 2008; Nikurashin and Ferrari 2013). However, inverse estimates and model simulations generally show an increase of the maximum northward abyssal flow as AABW crosses the ACC (e.g., Lumpkin and Speer 2007; Jayne 2009; Melet et al. 2014), indicating that the ACC is most likely a positive contributor to the northward dense water volume transport. This picture is consistent with isoneutral mixing (Iudicone et al. 2008a,b; Klocker and McDougall 2010) and near-field diapycnal mixing representing net sources of waters denser than  $28.11 \text{ kg m}^{-3}$  in the ACC region. We show that parameterized lee-wave-driven mixing, which largely dominates the estimated total water mass transformation by near-field

mixing and geothermal heating in the Southern Ocean, has an ambiguous role on the diabatic return of AABW; as well as augmenting the AABW input to northern basins, lee-wave radiation contributes to the homogenization of AABW and so facilitates its subsequent consumption by tidal mixing and geothermal heating. Additionally, we stress that diapycnal mixing can densify a water mass if the associated downward buoyancy flux is divergent within its density range; in particular, parameterized near-field mixing is a buoyancy sink for  $27.7\text{--}28.15\text{ kg m}^{-3}$  waters in the Southern Ocean. A portion of Lower Circumpolar Deep Water, mainly of North Atlantic origin, may thus be transformed into denser AABW class waters by topographically enhanced mixing in the ACC, short-circuiting the overturning from the upper to the lower branch (Naveira Garabato et al. 2007). This short circuit could provide for some of the interior consumption of deep waters and further intertwines both branches of the circulation.

Given fixed spatial distributions of energy dissipation and geothermal heat fluxes, the density field and topography of the ocean exert strong controls on the implied water mass transformation. Density classes that cover large portions of the seafloor are ideally placed to receive buoyancy from overlying water masses and the solid Earth through abyssal mixing and geothermal heating. In the present climate, AABW, which covers roughly two-thirds of the sea bottom (Fig. 5c; Johnson 2008), and its most voluminous variety ( $\gamma \approx 28.11\text{ kg m}^{-3}$ ) in particular are most efficiently consumed by such diabatic processes. Yet, under a different climate, rates of water mass transformation by geothermal heating and near-field mixing may strongly deviate from the present estimates. For instance, the geothermal circulation would be reduced in a more stratified abyssal ocean because individual density layers would have access to narrower seabed areas or, equivalently, because the stronger density gradients would require weaker diapycnal advection to balance the geothermal buoyancy gain (Emile-Geay and Madec 2009). In addition, if AABW upwelling is mostly confined to actively mixing ocean boundaries, the height distribution of the topographically complex seafloor may provide a strong constraint on the vertical extent and overall strength of the abyssal overturning.

Conversely, given fixed ocean topography and density structure, as well as fixed overall power available for mixing, transformation rates strongly depend on the specified spatial distribution of energy sinks. The vertical structure of the energy lost to the internal wave field has particularly important implications. In the deep ocean, away from strong gradients of the thermal

expansion coefficient, an increasing mixing energy with depth implies mostly buoyancy gain within a thin bottom layer and buoyancy loss elsewhere, driving strong, localized upwelling along topography. In contrast, a mixing energy that decreases with depth distributes buoyancy more evenly over the water column, driving only upward deep transport. On the other hand, a vertically homogenous mixing energy is highly efficient at driving a diabatic abyssal circulation, acting somewhat like a geothermal heat flux for the abyss and selectively consuming waters draping the ocean floor.

Important limitations to the present work must be underlined. First, uncertainty in the abyssal stratification, inherent to the sparse observations available at abyssal depths and especially close to the seabed, is a significant source of uncertainty for the estimated transformation rates. Second, the parameterization of near-field mixing relies on simplifying assumptions about the fraction of local internal wave dissipation, taken to be globally uniform for each wave type, and its vertical distribution, uniformly specified as an exponential decay from the bottom. In particular, the  $q_{LW}$  parameter and the overall amount of lee-wave dissipation remain poorly constrained so that the estimated transformation by breaking lee waves should be regarded as qualitatively representative of the real ocean but quantitatively accurate only to within a factor of  $\sim 3$ . On the other hand, the uncertainty in tidally forced diapycnal transports associated with  $q_{IT}$  and  $q_{ITAH}$  values is estimated to be a factor of  $\sim 1.5$ . Nonetheless, the impact of spatial variability in the mode partitioning of internal tide generation deserves further investigation. Third, presently used maps of internal wave generation rates contain uncertainty, primarily associated with imperfect knowledge of bathymetry and bottom flows and with shortcomings of the linear wave theory (Nycander 2005; Scott et al. 2011; Melet et al. 2013b), which may introduce further errors in the constructed dissipation fields. Inaccuracies in the field of geothermal heat fluxes (Goutorbe et al. 2011) could also bias the geothermal transformation estimate. However, it is the relatively well-constrained background flux of about  $55\text{ mW m}^{-2}$ , typical of abyssal plains, together with incrop areas that controls peak geothermal transports (see appendix B). Therefore, we do not expect uncertainties in geothermal heat fluxes to translate into strong biases in geothermal transformation rates. Next, it was assumed that one-sixth of the energy lost to the internal wave field contributes to irreversible mixing, except when this assumption led to unrealistic vertical diffusivities ( $>100\text{ cm}^2\text{ s}^{-1}$ ). Although the present assumption of a constant mixing efficiency allowed comparison with earlier studies, refinements could be considered in

future work (e.g., [St. Laurent et al. 2001](#); [Melet et al. 2013a](#)). Fifth, as opposed to numerical experiments, such static, climatological transformation estimates prohibit the response of stratification to vertical mixing and geothermal heating. In particular, this approach masks possible incompatibilities between the observed stratification and the estimated mixing levels, such as may result from overestimated mixing efficiencies. Further, the climatological approach neglects possible time correlations between fluctuations of hydrographic properties and mixing rates at the resolved spatial scales. Last, the present estimates do not allow quantification of the interplay between different processes. What would be the induced geothermal circulation if no mixing from lee waves and internal tides had contributed to shape the observed bottom density distribution? Such questions may find answers in OGCM studies ([Emile-Geay and Madec 2009](#)).

Nevertheless, we note that the climatological diapycnal transports diagnosed here are in broad agreement with earlier results from OGCM simulations using similar parameterizations or geothermal forcing (e.g., [Simmons et al. 2004](#); [Saenko and Merryfield 2005](#); [Emile-Geay and Madec 2009](#); [Oka and Niwa 2013](#); [Melet et al. 2014](#)), lending support to our conclusions. Such consistency also suggests that water mass transformation estimates provide a powerful tool to test parameterizations of diapycnal mixing and anticipate their impact on the simulated water mass structure and overturning circulation.

Whereas observations suggest a total AABW input to the Pacific, Indian, and Atlantic basins of about 20–30 Sv ([Ganachaud and Wunsch 2000](#); [Lumpkin and Speer 2007](#); [Talley et al. 2003](#); [Talley 2008, 2013](#)), herein-estimated contributions of near-field mixing and geothermal heating only sum to about 15 Sv of AABW upwelling north of 30°S. Far-field mixing from the breakdown of low-mode internal tides radiating away from generation sites could provide the required additional buoyancy supply. However, how and where non-local energy dissipation occurs is still largely unknown, so that gross assumptions must be made to represent this source of mixing ([Oka and Niwa 2013](#)). We explored the potential contribution of far-field mixing to deep-water mass conversion using idealized distributions of mixing energy. Depending mostly on the assumed vertical energy profile, AABW upwelling rates of 1 to 28 Sv were found compatible with a global power consumption of 0.85 TW. Such different rates of transformation imply radically different overturning circulations, highlighting the need for better constraints on the vertical distribution of remote energy dissipation and, ultimately, for an accurate three-dimensional mapping of energy sinks.

Other sources of mixing also require quantification. In particular, turbulence and entrainment in narrow passages, known to be important controls on the abyssal density distribution, could also be important contributors to AABW consumption ([Polzin et al. 1996](#); [Thurnherr and Speer 2003](#); [Bryden and Nurser 2003](#); [Thurnherr et al. 2005](#); [Huussen et al. 2012](#)). Candidate sources of mixing energy for the abyss also include the loss of balance of meso- to large-scale motions as they develop frontal instabilities near topography ([Zhai et al. 2010](#); [Dewar et al. 2011](#)) or in the interior ([Molemaker et al. 2010](#)).

Despite the limitations and uncertainties attached to the present transformation estimates and the correspondingly incomplete closure of the AABW life cycle, a qualitative picture of the diabatic, abyssal branch of the overturning can be proposed based on previously established and present results:

- 1) Intense buoyancy loss near Antarctica drives gravitational sinking of cold, relatively fresh surface waters. Aided by thermobaricity in their descent ([Killworth 1977](#); [McPhee 2003](#)), the sinking waters entrain surrounding waters, thereby increasing the dense water input to the deep Southern Ocean ([Orsi et al. 2002](#)).
- 2) Mixing with ambient waters and topographic constraints contribute to reduce the density of abyssal waters allowed to enter the ACC ([Orsi et al. 1999](#); [Johnson 2008](#)).
- 3) Further mixing occurs within the ACC, where turbulence from breaking lee waves consumes some of the densest AABW but also converts some of the overlying Circumpolar Deep Water into AABW class waters.
- 4) A fairly homogenous, weakly stratified bottom-water mass is transported northward into the Indo-Pacific and Atlantic basins at a rate of about 20–30 Sv. As it progresses and recirculates along the seafloor and through constrictive passages, AABW undergoes further homogenization and gradually gains buoyancy through deep mixing and heating from below.
- 5) Geothermal heating and abyssal mixing force AABW upwelling, preferentially along topographic features. The diabatic return of AABW occurs predominantly in regions of weak abyssal stratification and/or fractured topography.

*Acknowledgments.* We thank F. Roquet and A. Melet for helpful discussions and for sharing the tidal conversion estimates of [Nycander \(2005\)](#) and [Melet et al. \(2013b\)](#).

## APPENDIX A

**On the Role of the Nonlinearity of the Equation of State**

Locally dissipating internal tides and lee waves both induce a nonzero buoyancy flux into the global ocean: lee waves result in a volume-integrated neutral density loss of  $-2.0 \times 10^5 \text{ kg s}^{-1}$ , whereas internal tides cause a net neutral density gain of  $2.4 \times 10^6 \text{ kg s}^{-1}$  (Figs. 9a,b). Indeed, because of nonlinearity in the equation of state, mixing can be a net source or sink of neutral density and a strict balance between buoyancy gain and buoyancy loss need not be achieved.

We examine the role of nonlinearity by decomposing the total diapycnal transports  $T_{\text{mix}}$  into a linear component  $T_{\text{mix}}^{\text{lin}}$  and a nonlinear component  $T_{\text{mix}}^{\text{nonlin}} = T_{\text{mix}} - T_{\text{mix}}^{\text{lin}}$  (Fig. A1). Total buoyancy fluxes and transformation rates resulting from near-field mixing are shown for the regions north (Figs. A1b,c) and south (Figs. A1e,f) of 30°S. The impact of nonlinearity on diapycnal transports induced by parameterized near-field mixing appears relatively modest. Significant effects can be noted, however. First, upward transport across the  $28.11 \text{ kg m}^{-3}$  is increased by 1 Sv both north and south of 30°S, meaning that nonlinearity causes additional buoyancy gain (more precisely, neutral density loss) in the abyss. This effect is mostly explained by the increase with depth of the thermal expansion coefficient  $\alpha$  below about 2000 m (or  $\gamma = 27.8 \text{ kg m}^{-3}$ ) due to its pressure dependence (Figs. A1a,d; Palter et al. 2014).

Using (4) and (5), we can write the diapycnal velocity induced by nonlinear effects as

$$\omega^{\text{nonlin}} = \omega - \omega^{\text{lin}} = -(\partial_{\perp} \gamma)^{-1} [\partial_{\perp} (b \partial_{\theta} \rho) F^{\Theta} + \partial_{\perp} (b \partial_{S_A} \rho) F^{S_A}]. \quad (\text{A1})$$

Equation (A1) shows that net neutral density loss (corresponding to upwelling,  $\omega^{\text{nonlin}} < 0$ ) occurs when mixing transfers heat toward lower  $b \partial_{\theta} \rho = -\rho b \alpha$  or transfers salt toward lower  $b \partial_{S_A} \rho = \rho b \beta$  and conversely. Because the haline contraction coefficient  $\beta$  has relatively weak spatial variations relative to  $\alpha$ ,  $\omega^{\text{nonlin}}$  is dominated by the first term. Variations in the  $b$  factor are most significant south of 55°S (Iudicone et al. 2008b), so that its effect is secondary here except for some amplification of the nonlinear  $\alpha$  effect in the Southern Ocean (Fig. A1d). Thus, the increase of  $\alpha$  with depth in the abyss enhances neutral density loss and thereby the efficiency of AABW consumption. This shows up as increased buoyancy gain and upwelling for waters denser than  $27.8 \text{ kg m}^{-3}$  (Figs. A1b,c,e,f).

The tendency is reversed for lighter waters, however, since  $\alpha$  decreases sharply with depth within the tropical thermocline. For mode, intermediate, and tropical waters ( $\gamma \leq 27.5 \text{ kg m}^{-3}$ ), nonlinearity in the equation of state becomes a first-order effect. In the linear approximation, buoyancy gain by waters denser than  $25 \text{ kg m}^{-3}$  is exactly balanced by buoyancy loss for waters lighter than  $25 \text{ kg m}^{-3}$  (Figs. A1b,e). Including the full nonlinearity of the equation of state causes the buoyancy loss of waters lighter than  $27.2 \text{ kg m}^{-3}$  to amount to more than twice the buoyancy gain of denser waters. Indeed, by fluxing heat toward smaller  $\alpha$ , diapycnal mixing causes strong additional buoyancy loss (neutral density gain) in the upper ocean. Note that this effect will be greatly amplified when other sources of upper-ocean mixing are taken into account. Here, diapycnal temperature and salinity fluxes  $F^{\Theta}$  and  $F^{S_A}$  arise only from near-field mixing below the mixed layer driven by bottom-generated internal waves. Including mixed layer turbulence and processes such as direct wind mixing and surface-generated waves would greatly enhance the diapycnal fluxes  $F^{\Theta}$  and  $F^{S_A}$  and thereby the buoyancy loss and associated downwelling in (A1). Indeed, the herein-estimated, volume-integrated buoyancy loss owing to parameterized near-field mixing is  $1.9 \times 10^6 \text{ kg s}^{-1}$ , about 50 times weaker than that required to balance the global buoyancy gain from air–sea buoyancy fluxes (Schanze and Schmitt 2013; Palter et al. 2014).

## APPENDIX B

**On the Role of the Incrop Area**

The total geothermal and mixing-induced buoyancy fluxes entering the volume  $V(\gamma, +\infty)$  of waters denser than  $\gamma$ , defined by (17) and (18), can be written as the product between a mean buoyancy flux and the corresponding area of integration (Figs. B1a–c):

$$\begin{aligned} T_{\text{geo}}(\gamma) &= \partial_{\gamma} \iint_{I(\gamma, +\infty)} (-F_{\text{eq}}^{\gamma}) dA \\ &= \partial_{\gamma} \left[ \overline{F_{\text{geo}}^{\gamma}} \iint_{I(\gamma, +\infty)} dA \right], \quad \text{and} \quad (\text{B1}) \end{aligned}$$

$$T_{\text{mix}}(\gamma) = \partial_{\gamma} \iint_{A(\gamma) \cup O(\gamma, +\infty)} F_{\text{eq}}^{\gamma} dA = \partial_{\gamma} \left[ \overline{F_{\text{eq}}^{\gamma}} \iint_{A(\gamma) \cup O(\gamma, +\infty)} dA \right]. \quad (\text{B2})$$

Noting that, given the aspect ratio of the ocean, the surfaces bounding the considered volume from

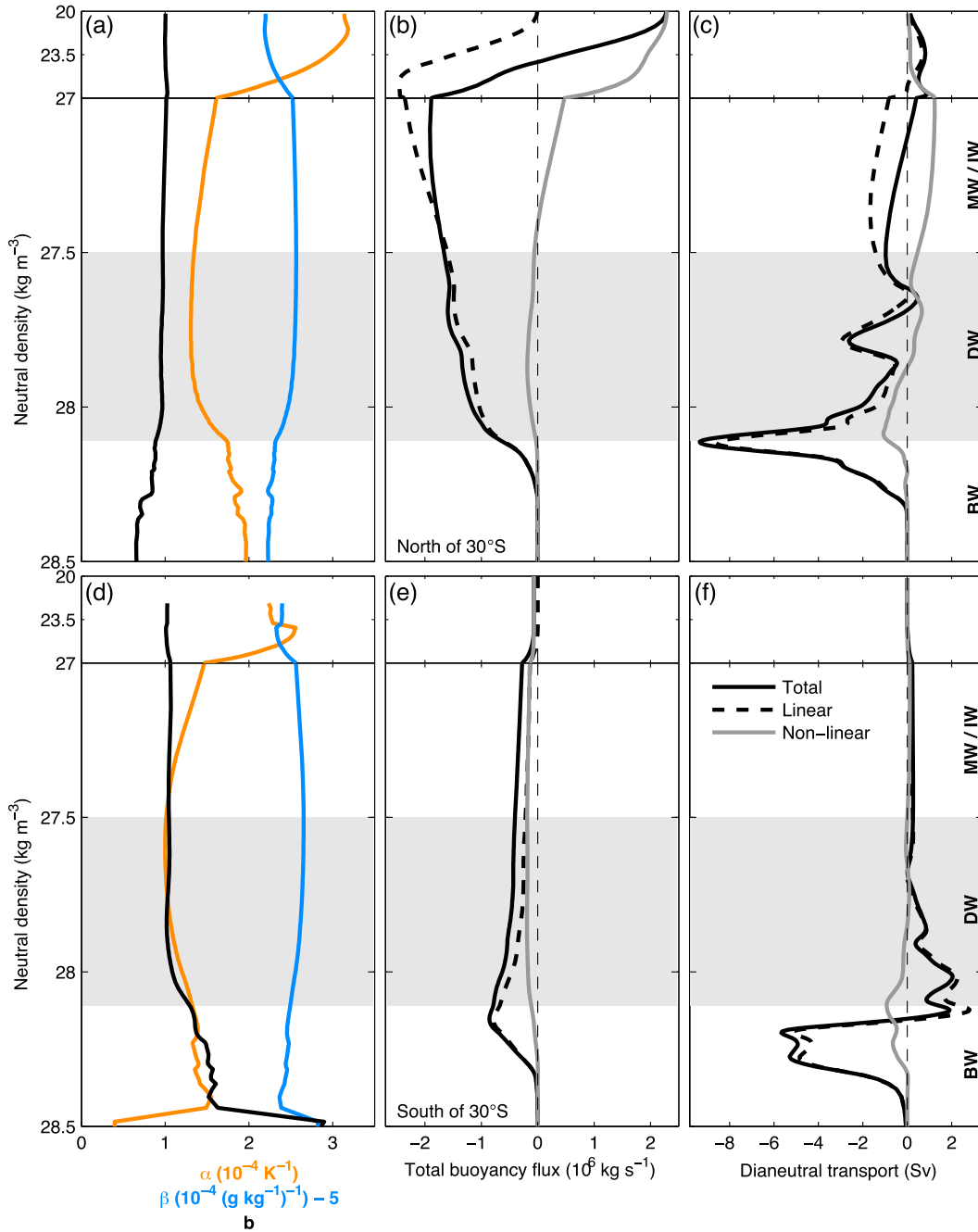


FIG. A1. Impact of the nonlinearity of the equation of state on water mass transformation by near-field mixing (top) north and (bottom) south of 30°S. (a),(d) Area-averaged thermal expansion coefficient  $\alpha$  (orange), haline contraction coefficient  $\beta$  (pale blue), and  $b$  factor (black) along neutral surfaces. A value of  $5 \times 10^{-4} (\text{g kg}^{-1})^{-1}$  is subtracted from  $\beta$  for display purposes. (b),(e) Total neutral density fluxes and (c),(f) dianeutral transports induced by near-field mixing including (black line) or excluding (dashed black line) the contribution of nonlinearity (gray line).

below and above have virtually equal areas  $\mathcal{A}$ , we can decompose  $T_{\text{geo}}$  and  $T_{\text{mix}}$  as the sum of a “mean flux term” and a “hypsometric term” as follows (Figs. B1d–f):

$$T_{\text{geo}}(\gamma) = \mathcal{A} \partial_{\gamma} \overline{F_{\text{geo}}^{\gamma}} + \overline{F_{\text{geo}}^{\gamma}} \partial_{\gamma} \mathcal{A} = \mathcal{A} \partial_{\gamma} \overline{F_{\text{geo}}^{\gamma}} + \overline{F_{\text{geo}}^{\gamma}} \mathcal{J}, \quad \text{and} \quad (\text{B3})$$

$$T_{\text{mix}}(\gamma) = \mathcal{A} \partial_{\gamma} \overline{F_{\text{eq}}^{\gamma}} + \overline{F_{\text{eq}}^{\gamma}} \partial_{\gamma} \mathcal{A} = \mathcal{A} \partial_{\gamma} \overline{F_{\text{eq}}^{\gamma}} + \overline{F_{\text{eq}}^{\gamma}} \mathcal{J}. \quad (\text{B4})$$

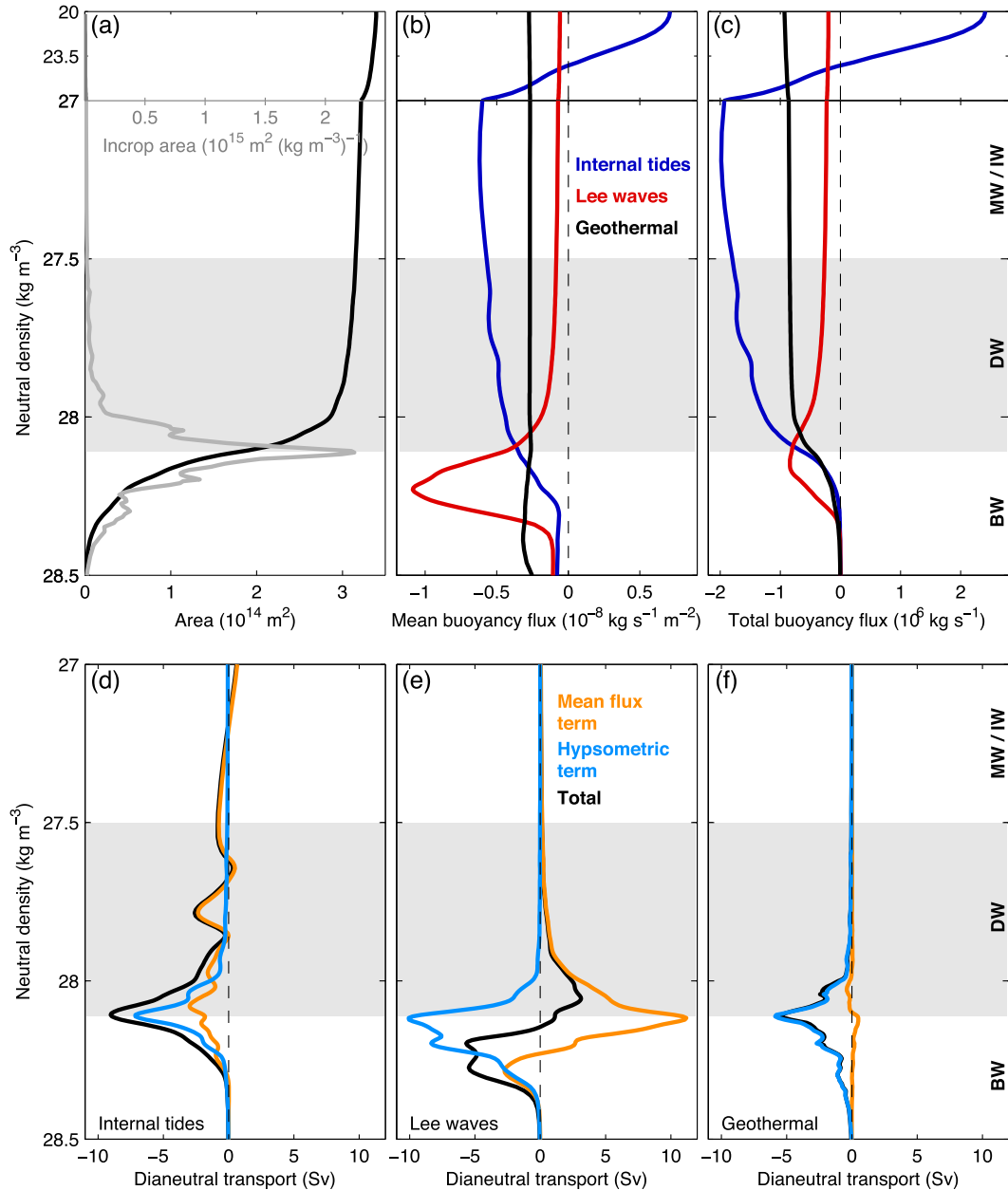


FIG. B1. Role of the incrop area on global water mass transformation by near-field mixing and geothermal heating. (a) Neutral density profile of  $\mathcal{A}$  (black) and its  $\gamma$  derivative  $\mathcal{J}$  (gray). (b) Area-averaged and (c) total neutral density fluxes induced by geothermal heating (black), near-field tidal mixing (blue), and lee-wave-driven mixing (red). Decomposition of global water mass transformation (black) by (d) near-field tidal mixing, (e) breaking lee waves, and (f) geothermal heating into mean flux (black) and hypsometric (pale blue) terms.

The second term, referred to as the hypsometric term, includes the factor  $\partial_\gamma \mathcal{A} = \mathcal{J}$ , which measures the reduction of the horizontal cross-sectional area of water volumes  $V(\gamma, +\infty)$  as one moves to higher  $\gamma$  or equivalently the incrop area of neutral density layers  $\mathcal{J}(\gamma)$ . Strictly speaking,  $\partial_\gamma \mathcal{A}$  reflects pseudohypsometry rather than hypsometry, in that it can be nonzero in the absence

of sloping topography (e.g., in the presence of sloping isopycnals on a flat bottom).

The mean geothermal buoyancy flux is almost constant throughout the ocean's neutral density range, so that the convergence of the total geothermal flux is almost exclusively controlled by the shrinking rate of the area  $\mathcal{A}$  (Figs. B1a–c). Therefore, one could replace the

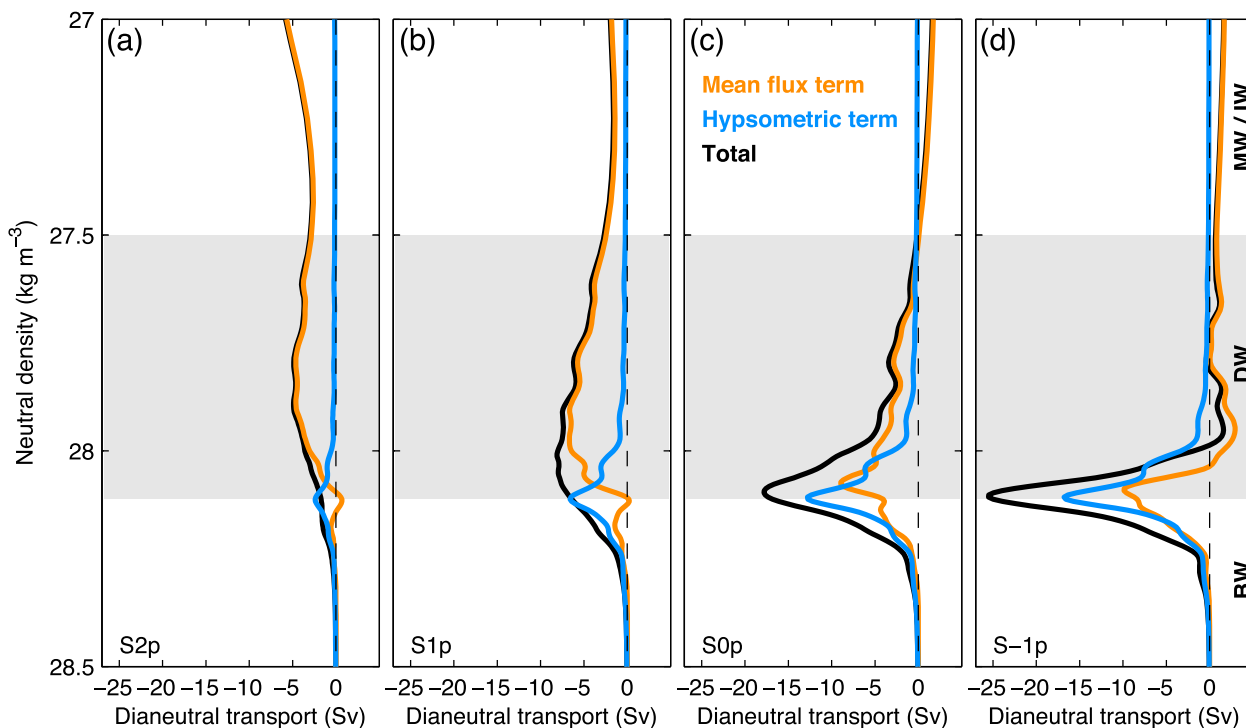


FIG. B2. Role of the incrop area on global water mass transformation by far-field tidal mixing. Decomposition of global water mass transformation by remotely dissipating internal tides (black) under scenarios (a) S2p, (b) S1p, (c) S0p, and (d) S-1p into mean flux (orange) and hypsometric (pale blue) terms.

spatially variable geothermal heat fluxes of Fig. 2c by a uniform heat flux without noticeably modifying the shape of the geothermal transformation curve; rates of geothermal upwelling are almost entirely determined by the incrop area (Fig. B1f). Near-field tidal mixing drives a mean buoyancy flux that decreases below the  $27.25 \text{ kg m}^{-3}$  neutral surface (Fig. B1b). The decrease in the mean flux adds to the sharp decrease in area  $\mathcal{A}$  near  $28.11 \text{ kg m}^{-3}$  to reinforce buoyancy deposition in the light AABW density class. Yet, the peak upwelling rate forced by internal tides at  $\gamma = 28.11 \text{ kg m}^{-3}$  remains controlled by the incrop area, as shown by the dominance of the hypsometric term at abyssal densities (Fig. B1d). On the other hand, the mean buoyancy flux associated with lee-wave-driven mixing exhibits a strong peak near  $28.25 \text{ kg m}^{-3}$  (Fig. B1b) so that the increase of the mean flux counteracts the hypsometric contribution to upwelling around  $\gamma = 28.11 \text{ kg m}^{-3}$  (Fig. B1e). The maximum upwelling rate implied by breaking lee waves is reached at higher densities, when the mean flux multiplying  $\mathcal{J}(\gamma)$  in the hypsometric term is still large.

The same decomposition between hypsometric and mean flux terms can be applied to transformation by far-field mixing (Fig. B2). Given the strong qualitative

similarity between horizontal distributions  $S_u$  and  $S_p$ , we choose to show only  $S_p$  scenarios. In the AABW density range, the hypsometric term systematically dominates over the mean flux term, whereas the reverse is true for neutral densities lower than  $28 \text{ kg m}^{-3}$ . This concurs with the strongest values of the incrop area being found within the  $28\text{--}28.3 \text{ kg m}^{-3}$  density range. Though the contribution of the mean flux term to upwelling at  $28.11 \text{ kg m}^{-3}$  reaches 5 Sv in scenario S0p and 9 Sv in scenario S-1p, most of the increase in AABW consumption going through scenarios S2 to S-1 can be explained by an increase in the mean buoyancy flux across the  $28.11 \text{ kg m}^{-3}$  neutral surface. Indeed, the strength of the buoyancy flux at  $\gamma = 28.11 \text{ kg m}^{-3}$  determines the actual efficiency of the hypsometry effect at the peak incrop area. But here, as in the case of near-field mixing and geothermal heating, the incrop area remains a dominant control on the structure of water mass transformation at abyssal densities, with waters of densities close to  $28.11 \text{ kg m}^{-3}$  being ideally placed to undergo rapid diabatic upwelling.

#### REFERENCES

- Adcroft, A., J. R. Scott, and J. Marotzke, 2001: Impact of geothermal heating on the global ocean circulation. *Geophys. Res. Lett.*, **28**, 1735–1738, doi:10.1029/2000GL012182.

- Bryden, H. L., and A. J. G. Nurser, 2003: Effects of strait mixing on ocean stratification. *J. Phys. Oceanogr.*, **33**, 1870–1872, doi:10.1175/1520-0485(2003)033<1870:EOSMOO>2.0.CO;2.
- Cummins, P. F., G. Holloway, and A. E. Gargett, 1990: Sensitivity of the GFDL ocean general circulation model to a parameterization of vertical diffusion. *J. Phys. Oceanogr.*, **20**, 817–830, doi:10.1175/1520-0485(1990)020<0817:SOTGOG>2.0.CO;2.
- Dewar, W. K., P. Berloff, and A. M. Hogg, 2011: Submesoscale generation by boundaries. *J. Mar. Res.*, **69**, 501–522, doi:10.1357/002224011799849345.
- Egbert, G. D., and R. D. Ray, 2000: Significant dissipation of tidal energy in the deep ocean inferred from satellite altimeter data. *Nature*, **405**, 775–778, doi:10.1038/35015531.
- Emile-Geay, J., and G. Madec, 2009: Geothermal heating, diapycnal mixing and the abyssal circulation. *Ocean Sci.*, **5**, 203–217, doi:10.5194/os-5-203-2009.
- Falahat, S., J. Nycander, F. Roquet, and M. Zarroug, 2014: Global calculation of tidal energy conversion into vertical normal modes. *J. Phys. Oceanogr.*, **44**, 3225–3244, doi:10.1175/JPO-D-14-0002.1.
- Ferrari, R., M. F. Jansen, J. F. Adkins, A. Burke, A. L. Stewart, and A. F. Thompson, 2014: Antarctic sea ice control on ocean circulation in present and glacial climates. *Proc. Natl. Acad. Sci. USA*, **111**, 8753–8758, doi:10.1073/pnas.1323922111.
- Ganachaud, A., and C. Wunsch, 2000: Improved estimates of global ocean circulation, heat transport and mixing from hydrographic data. *Nature*, **408**, 453–457, doi:10.1038/35044048.
- Gargett, A. E., 1984: Vertical eddy diffusivity in the ocean interior. *J. Mar. Res.*, **42**, 359–393, doi:10.1357/002224084788502756.
- Garrett, C., and W. Munk, 1972: Space-time scales of internal waves. *Geophys. Astrophys. Fluid Dyn.*, **3**, 225–264, doi:10.1080/03091927208236082.
- , and —, 1979: Internal waves in the ocean. *Annu. Rev. Fluid Mech.*, **11**, 339–369, doi:10.1146/annurev.fl.11.010179.002011.
- , and L. C. St. Laurent, 2002: Aspects of deep ocean mixing. *J. Oceanogr.*, **58**, 11–24, doi:10.1023/A:1015816515476.
- Gouretski, V. V., and K. P. Koltermann, 2004: WOCE global hydrographic climatology: A technical report. Berichte des Bundesamtes für Seeschifffahrt und Hydrographie 35/2004, 52 pp.
- Goutorbe, B., J. Poort, F. Lucazeau, and S. Raillard, 2011: Global heat flow trends resolved from multiple geological and geophysical proxies. *Geophys. J. Int.*, **187**, 1405–1419, doi:10.1111/j.1365-246X.2011.05228.x.
- Heywood, K. J., A. C. Naveira Garabato, and D. P. Stevens, 2002: High mixing rates in the abyssal Southern Ocean. *Nature*, **415**, 1011–1014, doi:10.1038/4151011a.
- Hofmann, M., and M. A. Morales Maqueda, 2009: Geothermal heat flux and its influence on the oceanic abyssal circulation and radiocarbon distribution. *Geophys. Res. Lett.*, **36**, L03603, doi:10.1029/2008GL036078.
- Huang, R. X., 1999: Mixing and energetics of the oceanic thermohaline circulation. *J. Phys. Oceanogr.*, **29**, 727–746, doi:10.1175/1520-0485(1999)029<0727:MAEOTO>2.0.CO;2.
- Huussen, T. N., A. C. Naveira-Garabato, H. L. Bryden, and E. L. McDonagh, 2012: Is the deep Indian Ocean MOC sustained by breaking internal waves? *J. Geophys. Res.*, **117**, C08024, doi:10.1029/2012JC008236.
- Ito, T., and J. Marshall, 2008: Control of lower-limb overturning circulation in the Southern Ocean by diapycnal mixing and mesoscale eddy transfer. *J. Phys. Oceanogr.*, **38**, 2832–2845, doi:10.1175/2008JPO3878.1.
- Iudicone, D., G. Madec, B. Blanke, and S. Speich, 2008a: The role of Southern Ocean surface forcings and mixing in the global conveyor. *J. Phys. Oceanogr.*, **38**, 1377–1400, doi:10.1175/2008JPO3519.1.
- , —, and T. J. McDougall, 2008b: Water-mass transformations in a neutral density framework and the key role of light penetration. *J. Phys. Oceanogr.*, **38**, 1357–1376, doi:10.1175/2007JPO3464.1.
- Jackett, D. R., and T. J. McDougall, 1997: A neutral density variable for the world's oceans. *J. Phys. Oceanogr.*, **27**, 237–263, doi:10.1175/1520-0485(1997)027<0237:ANDVFT>2.0.CO;2.
- Jayne, S. R., 2009: The impact of abyssal mixing parameterizations in an ocean general circulation model. *J. Phys. Oceanogr.*, **39**, 1756–1775, doi:10.1175/2009JPO4085.1.
- Johnson, G. C., 2008: Quantifying Antarctic Bottom Water and North Atlantic Deep Water volumes. *J. Geophys. Res.*, **113**, C05027, doi:10.1029/2007JC004477.
- Kelly, S. M., N. L. Jones, J. D. Nash, and A. F. Waterhouse, 2013: The geography of semidiurnal mode-1 internal-tide energy loss. *Geophys. Res. Lett.*, **40**, 4689–4693, doi:10.1002/grl.50872.
- Killworth, P. D., 1977: Mixing on the Weddell Sea continental slope. *Deep-Sea Res.*, **24**, 427–448, doi:10.1016/0146-6291(77)90482-9.
- Klocker, A., and T. J. McDougall, 2010: Influence of the nonlinear equation of state on global estimates of diapycnal advection and diffusion. *J. Phys. Oceanogr.*, **40**, 1690–1709, doi:10.1175/2010JPO4303.1.
- Koch-Larrouy, A., G. Madec, P. Bouruet-Aubertot, T. Gerkema, L. Bessières, and R. Molcard, 2007: On the transformation of Pacific Water into Indonesian Throughflow Water by internal tidal mixing. *Geophys. Res. Lett.*, **34**, L04604, doi:10.1029/2006GL028405.
- Kunze, E., and T. B. Sanford, 1996: Abyssal mixing: Where it is not. *J. Phys. Oceanogr.*, **26**, 2286–2296, doi:10.1175/1520-0485(1996)026<2286:AMWIIN>2.0.CO;2.
- , E. Firing, J. M. Hummon, T. K. Chereskin, and A. M. Thurnherr, 2006: Global abyssal mixing inferred from lowered ADCP shear and CTD strain profiles. *J. Phys. Oceanogr.*, **36**, 1553–1576, doi:10.1175/JPO2926.1.
- Ledwell, J. R., E. T. Montgomery, K. L. Polzin, L. C. St. Laurent, R. W. Schmitt, and J. M. Toole, 2000: Evidence for enhanced mixing over rough topography in the abyssal ocean. *Nature*, **403**, 179–182, doi:10.1038/35003164.
- Lumpkin, R., and K. Speer, 2007: Global ocean meridional overturning. *J. Phys. Oceanogr.*, **37**, 2550–2562, doi:10.1175/JPO3130.1.
- Marshall, J., D. Jamous, and J. Nilsson, 1999: Reconciling thermodynamic and dynamic methods of computation of water-mass transformation rates. *Deep-Sea Res.*, **46**, 545–572, doi:10.1016/S0967-0637(98)00082-X.
- Martini, K. I., M. H. Alford, E. Kunze, S. M. Kelly, and J. D. Nash, 2011: Observations of internal tides on the Oregon continental slope. *J. Phys. Oceanogr.*, **41**, 1772–1794, doi:10.1175/2011JPO4581.1.
- McDougall, T. J., 1984: The relative roles of diapycnal and isopycnal mixing on subsurface water mass conversion. *J. Phys. Oceanogr.*, **14**, 1577–1589, doi:10.1175/1520-0485(1984)014<1577:TRRODA>2.0.CO;2.
- , and P. M. Barker, 2011: Getting started with TEOS-10 and the Gibbs Seawater (GSW) oceanographic toolbox. SCOR/IAPSO WG127, 28 pp. [Available online at [www.teos-10.org/pubs/Getting\\_Started.pdf](http://www.teos-10.org/pubs/Getting_Started.pdf).]

- McPhee, M. G., 2003: Is thermobaricity a major factor in Southern Ocean ventilation? *Antarct. Sci.*, **15**, 153–160, doi:[10.1017/S0954102003001159](https://doi.org/10.1017/S0954102003001159).
- Melet, A., R. Hallberg, S. Legg, and K. Polzin, 2013a: Sensitivity of the ocean state to the vertical distribution of internal-tide-driven mixing. *J. Phys. Oceanogr.*, **43**, 602–615, doi:[10.1175/JPO-D-12-055.1](https://doi.org/10.1175/JPO-D-12-055.1).
- , M. Nikurashin, C. Muller, S. Falahat, J. Nycander, P. G. Timko, B. K. Arbic, and J. A. Goff, 2013b: Internal tide generation by abyssal hills using analytical theory. *J. Geophys. Res.*, **118**, 6303–6318, doi:[10.1002/2013JC009212](https://doi.org/10.1002/2013JC009212).
- , R. Hallberg, S. Legg, and M. Nikurashin, 2014: Sensitivity of the ocean state to lee wave–driven mixing. *J. Phys. Oceanogr.*, **44**, 900–921, doi:[10.1175/JPO-D-13-072.1](https://doi.org/10.1175/JPO-D-13-072.1).
- Molemaker, M. J., J. C. McWilliams, and X. Capet, 2010: Balanced and unbalanced routes to dissipation in an equilibrated Eady flow. *J. Fluid Mech.*, **654**, 35–63, doi:[10.1017/S0022112009993272](https://doi.org/10.1017/S0022112009993272).
- Müller, P., G. Holloway, F. Henyey, and N. Pomphrey, 1986: Nonlinear interactions among internal gravity waves. *Rev. Geophys.*, **24**, 493–536, doi:[10.1029/RG024i003p00493](https://doi.org/10.1029/RG024i003p00493).
- Munk, W., and C. Wunsch, 1998: Abyssal recipes II: Energetics of tidal and wind mixing. *Deep-Sea Res.*, **45**, 1977–2010, doi:[10.1016/S0967-0637\(98\)00070-3](https://doi.org/10.1016/S0967-0637(98)00070-3).
- Nash, J. D., E. Kunze, J. M. Toole, and R. W. Schmitt, 2004: Internal tide reflection and turbulent mixing on the continental slope. *J. Phys. Oceanogr.*, **34**, 1117–1134, doi:[10.1175/1520-0485\(2004\)034<1117:ITRATM>2.0.CO;2](https://doi.org/10.1175/1520-0485(2004)034<1117:ITRATM>2.0.CO;2).
- Naveira Garabato, A. C., K. L. Polzin, B. A. King, K. J. Heywood, and M. Visbeck, 2004: Widespread intense turbulent mixing in the Southern Ocean. *Science*, **303**, 210–213, doi:[10.1126/science.1090929](https://doi.org/10.1126/science.1090929).
- , D. P. Stevens, A. J. Watson, and W. Roether, 2007: Short-circuiting of the overturning circulation in the Antarctic Circumpolar Current. *Nature*, **447**, 194–197, doi:[10.1038/nature05832](https://doi.org/10.1038/nature05832).
- Nikurashin, M., and R. Ferrari, 2010a: Radiation and dissipation of internal waves generated by geostrophic motions impinging on small-scale topography: Theory. *J. Phys. Oceanogr.*, **40**, 1055–1074, doi:[10.1175/2009JPO4199.1](https://doi.org/10.1175/2009JPO4199.1).
- , and —, 2010b: Radiation and dissipation of internal waves generated by geostrophic motions impinging on small-scale topography: Application to the Southern Ocean. *J. Phys. Oceanogr.*, **40**, 2025–2042, doi:[10.1175/2010JPO4315.1](https://doi.org/10.1175/2010JPO4315.1).
- , and —, 2011: Global energy conversion rate from geostrophic flows into internal lee waves in the deep ocean. *Geophys. Res. Lett.*, **38**, L08610, doi:[10.1029/2011GL046576](https://doi.org/10.1029/2011GL046576).
- , and S. Legg, 2011: A mechanism for local dissipation of internal tides generated at rough topography. *J. Phys. Oceanogr.*, **41**, 378–395, doi:[10.1175/2010JPO4522.1](https://doi.org/10.1175/2010JPO4522.1).
- , and R. Ferrari, 2013: Overturning circulation driven by breaking internal waves in the deep ocean. *Geophys. Res. Lett.*, **40**, 3133–3137, doi:[10.1002/grl.50542](https://doi.org/10.1002/grl.50542).
- , —, N. Grisouard, and K. L. Polzin, 2014: The impact of finite-amplitude bottom topography on internal wave generation in the Southern Ocean. *J. Phys. Oceanogr.*, **44**, 2938–2950, doi:[10.1175/JPO-D-13-0201.1](https://doi.org/10.1175/JPO-D-13-0201.1).
- Niwa, Y., and T. Hibiya, 2011: Estimation of baroclinic tide energy available for deep ocean mixing based on three-dimensional global numerical simulations. *J. Oceanogr.*, **67**, 493–502, doi:[10.1007/s10872-011-0052-1](https://doi.org/10.1007/s10872-011-0052-1).
- Nurser, A. J. G., R. Marsh, and R. G. Williams, 1999: Diagnosing water mass formation from air–sea fluxes and surface mixing. *J. Phys. Oceanogr.*, **29**, 1468–1487, doi:[10.1175/1520-0485\(1999\)029<1468:DWMFFA>2.0.CO;2](https://doi.org/10.1175/1520-0485(1999)029<1468:DWMFFA>2.0.CO;2).
- Nycander, J., 2005: Generation of internal waves in the deep ocean by tides. *J. Geophys. Res.*, **110**, C10028, doi:[10.1029/2004JC002487](https://doi.org/10.1029/2004JC002487).
- , J. Nilsson, K. Döös, and G. Broström, 2007: Thermodynamic analysis of ocean circulation. *J. Phys. Oceanogr.*, **37**, 2038–2052, doi:[10.1175/JPO3113.1](https://doi.org/10.1175/JPO3113.1).
- Oka, A., and Y. Niwa, 2013: Pacific deep circulation and ventilation controlled by tidal mixing away from the sea bottom. *Nat. Commun.*, **4**, 2419, doi:[10.1038/ncomms3419](https://doi.org/10.1038/ncomms3419).
- Olbers, D., and M. Wenzel, 1989: Determining diffusivities from hydrographic data by inverse methods with applications to the circumpolar current. *Oceanic Circulation Models: Combining Data and Dynamics*, D. L. T. Anderson and J. Willebrand, Eds., NATO Science Series C, Vol. 284, Springer, 95–139.
- Orsi, A. H., G. C. Johnson, and J. L. Bullister, 1999: Circulation, mixing, and production of Antarctic Bottom Water. *Prog. Oceanogr.*, **43**, 55–109, doi:[10.1016/S0079-6611\(99\)00004-X](https://doi.org/10.1016/S0079-6611(99)00004-X).
- , W. M. Smethie Jr., and J. L. Bullister, 2002: On the total input of Antarctic waters to the deep ocean: A preliminary estimate from chlorofluorocarbon measurements. *J. Geophys. Res.*, **107**, doi:[10.1029/2001JC000976](https://doi.org/10.1029/2001JC000976).
- Osborn, T. R., 1980: Estimates of the local rate of vertical diffusion from dissipation measurements. *J. Phys. Oceanogr.*, **10**, 83–89, doi:[10.1175/1520-0485\(1980\)010<0083:EOTLRO>2.0.CO;2](https://doi.org/10.1175/1520-0485(1980)010<0083:EOTLRO>2.0.CO;2).
- Palter, J. B., S. M. Griffies, B. L. Samuels, E. D. Galbraith, A. Gnanadesikan, and A. Klocker, 2014: The deep ocean buoyancy budget and its temporal variability. *J. Climate*, **27**, 551–573, doi:[10.1175/JCLI-D-13-00016.1](https://doi.org/10.1175/JCLI-D-13-00016.1).
- Pollack, H. N., S. J. Hurter, and J. R. Johnson, 1993: Heat flow from the Earth’s interior: Analysis of the global data set. *Rev. Geophys.*, **31**, 267–280, doi:[10.1029/93RG01249](https://doi.org/10.1029/93RG01249).
- Polzin, K. L., 2009: An abyssal recipe. *Ocean Modell.*, **30**, 298–309, doi:[10.1016/j.ocemod.2009.07.006](https://doi.org/10.1016/j.ocemod.2009.07.006).
- , K. G. Speer, J. M. Toole, and R. W. Schmitt, 1996: Intense mixing of Antarctic Bottom Water in the equatorial Atlantic Ocean. *Nature*, **380**, 54–57, doi:[10.1038/380054a0](https://doi.org/10.1038/380054a0).
- , J. M. Toole, J. R. Ledwell, and R. W. Schmitt, 1997: Spatial variability of turbulent mixing in the abyssal ocean. *Science*, **276**, 93–96, doi:[10.1126/science.276.5309.93](https://doi.org/10.1126/science.276.5309.93).
- Saenko, O. A., and W. J. Merryfield, 2005: On the effect of topographically enhanced mixing on the global ocean circulation. *J. Phys. Oceanogr.*, **35**, 826–834, doi:[10.1175/JPO2722.1](https://doi.org/10.1175/JPO2722.1).
- , X. Zhai, W. J. Merryfield, and W. G. Lee, 2012: The combined effect of tidally and eddy-driven diapycnal mixing on the large-scale ocean circulation. *J. Phys. Oceanogr.*, **42**, 526–538, doi:[10.1175/JPO-D-11-0122.1](https://doi.org/10.1175/JPO-D-11-0122.1).
- Schanze, J. J., and R. W. Schmitt, 2013: Estimates of cabbeling in the global ocean. *J. Phys. Oceanogr.*, **43**, 698–705, doi:[10.1175/JPO-D-12-0119.1](https://doi.org/10.1175/JPO-D-12-0119.1).
- Scott, R. B., J. A. Goff, A. C. Naveira Garabato, and A. J. G. Nurser, 2011: Global rate and spectral characteristics of internal gravity wave generation by geostrophic flow over topography. *J. Geophys. Res.*, **116**, C09029, doi:[10.1029/2011JC007005](https://doi.org/10.1029/2011JC007005).
- Sheen, K. L., and Coauthors, 2013: Rates and mechanisms of turbulent dissipation and mixing in the Southern Ocean: Results from the Diapycnal and Isopycnal Mixing Experiment in the Southern Ocean (DIMES). *J. Geophys. Res. Oceans*, **118**, 2774–2792, doi:[10.1002/jgrc.20217](https://doi.org/10.1002/jgrc.20217).
- Simmons, H. L., S. R. Jayne, L. C. St. Laurent, and A. J. Weaver, 2004: Tidally driven mixing in a numerical model of the ocean

- general circulation. *Ocean Modell.*, **6**, 245–263, doi:[10.1016/S1463-5003\(03\)00011-8](https://doi.org/10.1016/S1463-5003(03)00011-8).
- Sloyan, B. M., 2005: Spatial variability of mixing in the Southern Ocean. *Geophys. Res. Lett.*, **32**, L18603, doi:[10.1029/2005GL023568](https://doi.org/10.1029/2005GL023568).
- Stein, C. A., and S. Stein, 1992: A model for the global variation in oceanic depth and heat flow with lithospheric age. *Nature*, **359**, 123–129, doi:[10.1038/359123a0](https://doi.org/10.1038/359123a0).
- St. Laurent, L. C., and C. Garrett, 2002: The role of internal tides in mixing the deep ocean. *J. Phys. Oceanogr.*, **32**, 2882–2899, doi:[10.1175/1520-0485\(2002\)032<2882:TROITI>2.0.CO;2](https://doi.org/10.1175/1520-0485(2002)032<2882:TROITI>2.0.CO;2).
- , and J. D. Nash, 2004: An examination of the radiative and dissipative properties of deep ocean internal tides. *Deep-Sea Res.*, **51**, 3029–3042, doi:[10.1016/j.dsr2.2004.09.008](https://doi.org/10.1016/j.dsr2.2004.09.008).
- , J. M. Toole, and R. W. Schmitt, 2001: Buoyancy forcing by turbulence above rough topography in the abyssal Brazil basin. *J. Phys. Oceanogr.*, **31**, 3476–3495, doi:[10.1175/1520-0485\(2001\)031<3476:BFBTAR>2.0.CO;2](https://doi.org/10.1175/1520-0485(2001)031<3476:BFBTAR>2.0.CO;2).
- , H. L. Simmons, and S. R. Jayne, 2002: Estimating tidally driven mixing in the deep ocean. *Geophys. Res. Lett.*, **29**, 2106, doi:[10.1029/2002GL015633](https://doi.org/10.1029/2002GL015633).
- Talley, L. D., 2008: Freshwater transport estimates and the global overturning circulation: Shallow, deep and through-flow components. *Prog. Oceanogr.*, **78**, 257–303, doi:[10.1016/j.pocean.2008.05.001](https://doi.org/10.1016/j.pocean.2008.05.001).
- , 2013: Closure of the global overturning circulation through the Indian, Pacific, and Southern Oceans: Schematics and transports. *Oceanography*, **26**, 80–97, doi:[10.5670/oceanog.2013.07](https://doi.org/10.5670/oceanog.2013.07).
- , J. L. Reid, and P. E. Robbins, 2003: Data-based meridional overturning streamfunctions for the global ocean. *J. Climate*, **16**, 3213–3226, doi:[10.1175/1520-0442\(2003\)016<3213:DMOSFT>2.0.CO;2](https://doi.org/10.1175/1520-0442(2003)016<3213:DMOSFT>2.0.CO;2).
- Thurnherr, A. M., and K. G. Speer, 2003: Boundary mixing and topographic blocking on the mid-Atlantic ridge in the South Atlantic. *J. Phys. Oceanogr.*, **33**, 848–862, doi:[10.1175/1520-0485\(2003\)33<848:BMATBO>2.0.CO;2](https://doi.org/10.1175/1520-0485(2003)33<848:BMATBO>2.0.CO;2).
- , L. C. St. Laurent, K. G. Speer, J. M. Toole, and J. R. Ledwell, 2005: Mixing associated with sills in a canyon on the midocean ridge flank. *J. Phys. Oceanogr.*, **35**, 1370–1381, doi:[10.1175/JPO2773.1](https://doi.org/10.1175/JPO2773.1).
- Toggweiler, J. R., and B. Samuels, 1995: Effect of Drake Passage on the global thermohaline circulation. *Deep-Sea Res.*, **42**, 477–500, doi:[10.1016/0967-0637\(95\)00012-U](https://doi.org/10.1016/0967-0637(95)00012-U).
- Toole, J. M., R. W. Schmitt, and K. L. Polzin, 1994: Estimates of diapycnal mixing in the abyssal ocean. *Science*, **264**, 1120–1123, doi:[10.1126/science.264.5162.1120](https://doi.org/10.1126/science.264.5162.1120).
- Walin, G., 1982: On the relation between sea-surface heat flow and thermal circulation in the ocean. *Tellus*, **34A**, 187–195, doi:[10.1111/j.2153-3490.1982.tb01806.x](https://doi.org/10.1111/j.2153-3490.1982.tb01806.x).
- Waterhouse, A. F., and Coauthors, 2014: Global patterns of diapycnal mixing from measurements of the turbulent dissipation rate. *J. Phys. Oceanogr.*, **44**, 1854–1872, doi:[10.1175/JPO-D-13-0104.1](https://doi.org/10.1175/JPO-D-13-0104.1).
- Waterman, S., A. C. Naveira Garabato, and K. L. Polzin, 2013: Internal waves and turbulence in the Antarctic Circumpolar Current. *J. Phys. Oceanogr.*, **43**, 259–282, doi:[10.1175/JPO-D-11-0194.1](https://doi.org/10.1175/JPO-D-11-0194.1).
- , K. L. Polzin, A. C. Naveira Garabato, K. L. Sheen, and A. Forryan, 2014: Suppression of internal wave breaking in the Antarctic Circumpolar Current near topography. *J. Phys. Oceanogr.*, **44**, 1466–1492, doi:[10.1175/JPO-D-12-0154.1](https://doi.org/10.1175/JPO-D-12-0154.1).
- Wright, C. J., R. B. Scott, P. Ailliot, and D. Furnival, 2014: Lee wave generation rates in the deep ocean. *Geophys. Res. Lett.*, **41**, 2434–2440, doi:[10.1002/2013GL059087](https://doi.org/10.1002/2013GL059087).
- Wunsch, C., and R. Ferrari, 2004: Vertical mixing, energy, and the general circulation of the oceans. *Annu. Rev. Fluid Mech.*, **36**, 281–314, doi:[10.1146/annurev.fluid.36.050802.122121](https://doi.org/10.1146/annurev.fluid.36.050802.122121).
- Zhai, X., H. L. Johnson, and D. P. Marshall, 2010: Significant sink of ocean-eddy energy near western boundaries. *Nat. Geosci.*, **3**, 608–612, doi:[10.1038/ngeo943](https://doi.org/10.1038/ngeo943).